Refining the active phases of silver/nickle-based catalysts achieves a highly-selective reduction of nitrate to ammonium at low overpotential

Yingyang Jiang [a,1], Deqing Kong [a,1], Longlong Huang [a], Shilu Wu [a], Peng Xu [a], Ling Ye [a], Xuemei Zhou [a], Jinjie Qian [a], Hao Tang [a], Yongjie Ge [a,*], Jia Guan [b,*], Zhi Yang [a,*], Huagui Nie [a,*]

[a] Key Laboratory of Carbon Materials of Zhejiang, College of Chemistry and Materials Engineering, Wenzhou University, Wenzhou 325035, PR China
[b] Institute of New Materials & Industrial Technology, Wenzhou University, Wenzhou, Zhejiang 325035, PR China

ARTICLE INFO

ABSTRACT

The electrocatalytic conversion of NO_3^- to NH_3 (NO_3RR) with elevated activity and exceptional selectivity at low potential remains a formidable challenge. Herein, the A-Ag@Ni/Ni(OH)$_2$ NWs with atomic-level Ag/Ni interfaces were synthesized via electrochemical activation of Ag@Ni/Ni(OH)$_2$ NWs at −1.05 V *vs.* RHE for 1 hour, and subsequently employed for electrocatalytic NO_3RR. Specially, Ag sites could afford active centers for the adsorption of NO_3^- and convert it to NO_2^-. Furthermore, Ni/Ni(OH)$_2$ sites as vibrant centers for electrocatalytic H_2O splitting, generating atomic H on the catalyst surface (H_{ads}), thereby facilitating the rapid conversion of NO_2^- to NH_3 via the H_{ads}-mediated pathway. DFT calculations further substantiate that the H_{ads}-mediated pathway is thermodynamically more favorable than the electron reduction pathway, the former of which facilitates the generation of NH_3 and is an energy-efficient process, thus, the A-Ag@Ni/Ni(OH)$_2$ NWs show outstanding electrocatalytic activity and selectivity for NO_3^--to-NH_3 transformation at low potential.

1. Introduction

Ammonia (NH_3) plays a crucial role as a fundamental chemical in industries such as fertilizer, textiles, pharmaceuticals, and more. Furthermore, its classification as a clean energy carrier stems from its hydrogen-rich nature, making it a carbon-free alternative [1–3]. At present, the industrial-scale synthesis of NH_3 predominantly depends on the energy-intensive Haber–Bosch process. This process involves the reaction between N_2 and H_2 at elevated temperatures (400–500 °C) and high pressures (150–300 atm) [4]. Considering energy-saving perspectives, the electroreduction of ambient N_2 (NRR) emerges as a compelling alternative strategy. However, it is hindered by low selectivity and activity, attributed to the highly stable N≡N triple bond (941 kJ mol^{-1}) and limited water solubility [5,6]. On the contrary, the electrocatalytic reduction of NO_3^- (NO_3RR) stands out as a logical approach for NH_3 synthesis. This is particularly justified by the relatively low dissociation energy of the N=O bond in NO_3^- (204 kJ mol^{-1}) [7,8]. Furthermore, NO_3^- is abundantly present as a pollutant in agricultural and industrial wastewater [9]. Therefore, the development of NO_3RR presents a green pathway for synthesizing NH_3 and a promising solution to address environmental pollution challenges.

The NO_3RR process entails the transfer of nine protons and eight electrons ($NO_3^- + 9 H^+ + 8e^- \rightarrow NH_3 + 3 H_2O$), and it may unavoidably produce some undesired byproducts, such as nitrogen oxyanions and dinitrogen [7,10]. In this regard, to improve NO_3^- to NH_3 efficiently and selectively, there is a distinct need for the strategic design and development of catalysts with superior activity and efficiency in promoting the NO_3RR. The catalytic mechanism of traditional non-noble metal catalysts such as Cu is usually based on an electron reduction pathway. Namely, the electrons directly reduce NO_3^- to NH_3 through intermediates such as NO_2^-, NO, NOH, NHOH, NH_2OH, and so on [11–14]. However, these catalysts exhibit poor selectivity for ammonia synthesis at low potentials, mainly due to the more straightforward conversion of intermediate NO to nitrogen at low potentials [15–17].

Moreover, the mediation of adsorbed atomic hydrogen (H_{ads}) is also instrumental in facilitating the NO_3RR. As a potent reducing agent, H_{ads} can gradually reduce the adsorbed NO_2^- to NH_3 via intermediates such as $NO_2^-_{ads}$, NO_{ads}, N_{ads}, NH_{ads}, and NH_{2ads} [18–20]. Since the formation of the N–H bond mediated by H_{ads} is more kinetically favorable than the formation of the N–N bond [19,21], an augmented adsorption of H_{ads} on

* Corresponding authors.
E-mail addresses: geyongjie1220@126.com (Y. Ge), guanjia@wzu.edu.cn (J. Guan), yang201079@126.com (Z. Yang), huaguinie@126.com (H. Nie).
[1] These authors contributed equally to this work.

the catalyst surface can significantly enhance the synthesis of NH_3. In addition, the H_{ads}-mediated pathway is more energy-efficient for NH_3 synthesis because the process usually occurs at a low overpotential [21]. Notably, catalysts based on precious metals such as Pd, Pt, and Ru have attracted considerable attention for electrochemically converting NO_3^- to NH_3 owing to their advantageous hydrogen adsorption capabilities [18,22]. However, the precious metal catalysts prove less than ideal for NO_3RR due to both resource scarcity and high costs. The exploration of alternative catalysts has led to the investigation of non-precious metals, including Ni and Co-based catalysts [23–25]. Despite these catalysts demonstrate specific catalytic performances, their activity towards NO_3RR remains restricted by the conversion of NO_3^- to NO_2^-, primarily attributed to their significant catalytic activity for water splitting, which restricts the adsorption of NO_3^- [26]. For the heterogeneous catalysis reaction, the adsorption of NO_3^- on the catalysts serves as a prerequisite [27].

Among metal catalysts, silver (Ag)-based catalysts stand out for their exceptional electrocatalytic activity in converting NO_3^- into NO_2^- [26]. Furthermore, the utilization of one-dimensional nanowire structures, distinguished by their exceptional conductivity, adds to the attractiveness of electrocatalysis [28–30]. Thus, in this work, we selected silver nanowires (Ag NWs) as a template for crafting the catalyst for NO_3RR. The decision to integrate the $Ni/Ni(OH)_2$ heterostructure as a sub-component of the catalysts was motivated by its proven high activity in the hydrogen evolution reaction (HER) [31,32]. The electrocatalytic tests, kinetic studies, radical scavenging experiments and theoretical calculations reveal that the Ag phases as active sites for adsorbing NO_3^- and converting it to NO_2^-. Meanwhile, the $Ni/Ni(OH)_2$ phase forming atomic H on the catalyst surface. The resulting H_{ads} promotes the NO_2^- and other intermediates convert into NH_3 through the H_{ads}-mediated pathway. Benefiting from the synergistic effect between the Ag phase and Ni phase, the as-synthesized catalyst exhibits an efficient NO_3^--to-NH_3 conversion with a high faraday efficiency (FE) of 92.3%, high NH_3 yield rate of 2507.3 µg h^{-1} cm^{-2}, and high selectivity of 95.14% in 0.1 M KNO_3 + 1 M KOH solution at -0.05 V *vs*. RHE (Reversible hydrogen electrode).

2. Experimental section

2.1. Materials

$AgNO_3$ (AR), $CuCl_2$ (AR), acetone (AR), PVP (K-30, GR), and ethylene glycol were procured from Sinopharm Chemical Reagent Co., Ltd. KOH (ACS), Nickel(II) acetylacetonate (ACP), oleylamine (AR), n-hexane (GC) were obtained from Aladdin. Additionally, NaOH (ACS), $NaNO_2$ (AR), KNO_3 (ACS), Salicylic acid (AR), Sulfanilamide (ACS) were purchased from Sigma-Aldrich. All chemicals were utilized without further purification. Ultrapure water ($\geq$18.2 MΩ cm), obtained through an Elix5-Milli-Q ultrapure water system, was utilized consistently in all experiments.

2.2. Synthesis of Ag NWs

Ag NWs were synthesized using the polyol reduction method as reported in prior studies [33,34]. In briefly, ethylene glycol (20 mL), PVP (166.7 mg), and $CuCl_2$ in ethylene glycol (35 µL, 0.01 M) were added into a 250 mL round-bottom flask in an oil bath while magnetic stirring. The flask was then ramped to a temperature of 165 ^{o}C and kept for 10 min, followed by the addition of $AgNO_3$ in ethylene glycol (70 µL, 0.01 M) and maintaining for another 30 min. After that, additional $AgNO_3$ in ethylene glycol (5 mL, 0.1 M) was injected within 10 min using a syringe pump, following by heating at 165 ^{o}C for additional 60 min. The reaction was quenched by cooling the flask in a room temperature water bath. The resultant Ag NWs were then washed with acetone once and ethanol three times, and then stored in ethanol, forming a bulk dispersion (1 mg/mL).

2.3. Synthesis of $Ag@Ni/Ni(OH)_2$ NWs

For the preparation of $Ag@Ni/Ni(OH)_2$ NWs, 10 mg of Ag NWs were dispersed in a 10 mL solution containing 30 mM Nickel(II) acetylacetonate oleylamine solution The mixture was heated at 90 ^{o}C for 10 min under vigorous stirring in an Ar atmosphere. Subsequently, the temperature was increased to 200 ^{o}C, and the reaction proceeded for 1 h. The reaction temperature and heating rate can be regulated by adjusting both the heating temperature and power of the oil bath (Zhengzhou Greatwall Technology Industry and Trade Co., LTD, HWCL-5). The reaction was terminated by cooling the flask in a room-temperature water bath. The resulting $Ag@Ni/Ni(OH)_2$ NWs were subjected to three washes with a mixture of ethanol, n-hexane, and acetone. Subsequently, the $Ag@Ni/Ni(OH)_2$ NWs were stored in ethanol, creating a concentrated dispersion with a concentration of 3 mg/mL.

2.4. Synthesis of $A-Ag@Ni/Ni(OH)_2$ NWs

$A-Ag@Ni/Ni(OH)_2$ NWs were obtained through the electrochemical activation of $Ag@Ni/Ni(OH)_2$ NWs using a three-electrode system at a potential of -1.05 V *vs*. RHE for 1 h. Here, a carbon paper (CP) loaded with $Ag@Ni/Ni(OH)_2$ NWs served as the working electrode, while Ag/AgCl (saturated KCl) and a platinum mesh were used as the reference and counter electrodes, respectively. The preparation process of the working electrode is as follows: a suspension of $Ag@Ni/Ni(OH)_2$ NWs (3 mg/mL, 200 µL) was cast onto a clean CP with an area of 1×1 cm^2, dried in vacuum at room temperature, and then 50 µL of 1% Nafion emulsion was added. The mass loading of $Ag@Ni/Ni(OH)_2$ NWs is 0.6 mg cm^{-2}.

2.5. Material characterization

SEM analysis was conducted using a scanning electron microscope (Nova Nano SEM 200, FEI, USA). TEM images were acquired using transmission electron microscope (FEIT Tecnai G2F 20 system), utilizing copper grids sourced from JEOL, Japan. X-ray photoelectron spectroscopy (XPS) was collected using an ultrahigh-vacuum setup (SES 2002, Gammadata-Scienta) equipped with a monochromatic Al Kα X-ray source. It's worth noting that during the SEM and TEM characterization processes, $A-Ag@Ni/Ni(OH)_2$ NWs need to be transferred from carbon paper to silicon wafers and copper meshes, respectively.

The Raman spectra of $Ag@Ni/Ni(OH)_2$ NWs and $A-Ag@Ni/Ni(OH)_2$ NWs were collected on the confocal Raman microscope. Briefly, the electrolytic cell was homemade by Teflon with a piece of round quartz glass as a cover to protect the objective (Figure S1). The Au electrode modified with the catalyst was used as the working electrode, Pt wire and Ag/AgCl electrode as the counter and reference electrodes, respectively. The surface of the working electrode was positioned 100–200 µm from the glass window. A laser of 785 nm and 50 mW vertically crossed the glass and was focused on the electrode surface with a 50× objective. The average acquisition time for each spectrum was 5 min. UV–visible absorption spectra were measured by UV-1800 (Shimadzu, Japan). Fourier-transform infrared (FT-IR) spectra were acquired using an IRTracer-100 spectrometer (Shimadzu, Japan). Nuclear magnetic resonance (NMR) spectroscopy was conducted on an AVANCE III AV500 spectrometer.

2.6. Electrochemical tests

The electrocatalytic tests were conducted utilizing a standard three-electrode system connected to the CHI 660E electrochemical workstation (CHI Instrument, China) within a conventional H-type cell. The catalysts supported by carbon paper, Ag/AgCl (saturated KCl), and platinum mesh were used as the working electrode, reference, and counter electrodes, respectively. The working electrode is prepared as follows: A suspension of the as-synthesized catalysts was cast onto a

clean carbon paper (CP) with an area of 1×1 cm^{-2}, dried under vacuum at room temperature, and then 50 μL of 1% Nafion emulsion was added. The mass loading of the as-synthesized catalysts is 0.6 mg cm^{-2}.

The electrolytes comprised Ar-saturated 1 M KOH with varying concentrations of NO$_3^-$ or NO$_2^-$. The LSV curves were recorded at a scan rate of 10 mV·s^{-1} and were not IR corrected. The Tafel slopes were extracted from nearly static LSV data. All potentials were calibrated to the RHE reference scale through the application of a specific formula $E_{RHE} = E_{Ag/AgCl} + 0.204$ V $+ 0.0591 \times$ pH. The current density was normalized to the geometric electrode area of approximately 1 cm^2. Potentiostatic measurements were conducted over a duration of 1 hour in a 30 mL cathode electrolyte, followed by storage at 4 °C (for no more than 2 days) before subsequent analysis. Furthermore, the electrolyte solution was collected and analyzed for NH$_3$ production after each hour of electrolysis to evaluate the prolonged stability of A-Ag@Ni/Ni(OH)$_2$ NWs for NO$_3$RR. To ensure consistency, a new electrolyte solution was employed for every cycle of one-hour electrolysis. The C$_{dl}$ was determined by conducting CV scanning within a non-faradaic potential window at 10–70 mV·s^{-1} scan rates. The plot of the differences between the capacitive anode and cathode currents $[(j_a–j_c)/2]$ at a set potential against the CV scan rates exhibits a linear relationship, with the slope representing C$_{dl}$. Electrochemical impedance spectroscopy (EIS) tests were conducted using an Auto lab potentiostat (Metrohm, Switzerland). EIS was performed at different applied potentials *vs.* RHE across the frequency range of 10^{-2}-10^{-5} Hz.

2.7. Determination of ion concentrations

2.7.1 NH$_4^+$ quantification.
The generated NH$_3$ was quantitatively assessed using the indophenol blue method [35,36]. Usually, a specific volume of electrolyte was extracted from the reaction cell and diluted to 2 mL. Subsequently, 1 M NaOH solution containing 5 wt% of citrate dihydrate and salicylic acid (2 mL), stored at 4 °C, were combined with 1 mL of freshly prepared 0.05 M NaClO for the color reaction. The resulting mixture was briefly shaken to ensure thorough mixing of the components. Subsequently, 1 wt% sodium nitroferricyanide solution (0.2 mL), stored at 4 °C, was introduced to initiate the color reaction. The resulting solution was analyzed after a 2-hour incubation period at room temperature using an ultraviolet-visible (UV-Vis) spectrophotometer. The absorbance at 655 nm was employed for determining the concentration of NH$_3$. For quantifying the amount of NH$_3$, a calibration curve was constructed utilizing a standard NH$_4$Cl solution in 1 M KOH.

2.7.2 NO$_2^-$ quantification.
A dedicated color reagent for NO$_2^-$ quantification was formulated by combining 0.08 g of N-(1-naphthyl) ethylenediamine dihydrochloride, 4 mL of phosphoric acid (85 wt%, ρ =1.7 g/mL) and sulfonamide (1.6 g) were mixed with 20 mL of deionized water[37]. In a standard colorimetric test, 1 mL of HCl (1 M) was initially added to 5 mL of diluted post-electrolysis electrolytes, followed by the addition of 0.1 mL of the color reagent. The mixture was then shaken to achieve a uniform solution. The UV-Vis absorbance at 540 nm was measured at room temperature after 30 minutes. The quantity of NO$_2^-$ was identified by a calibration curve constructed with NaNO$_2$ solutions.

2.8. Calculation of the NH$_3$ yield rate and Faradaic efficiency

Considering the consumption of eight electrons to produce one NH$_3$ molecule, the Faradaic Efficiency (FE$_{NH_3}$) and NH$_3$ yield rate (Y$_{NH_3}$) were calculated using the following Eqs. (1) and (2): where F represents the Faraday constant (96485 C mol^{-1}), Q denotes the total charge passing the electrode, c_{NH_3} signifies the molar concentration of detected NH$_3$, V_{NH_3} represents the volume of the electrolytes (30 mL), A is the geometric area of the electrode (1 cm^2), and t stands for the reaction time.

$$FE_{NH_3} = \frac{8V_{NH_3}c_{NH_3}F}{Q} \qquad Y_{NH_3} = \frac{V_{NH_3}c_{NH_3}}{At}$$

Considering that two electrons are utilized to generate one NO$_2^-$ molecule, the FE of NO$_2^-$ can be calculated using the following formula:

$$FE_{NO_2^-} = \frac{2V_{NO_2^-}c_{NO_2^-}F}{Q}$$

Here, $c_{NO_2^-}$ represents the molar concentration of detected NO$_2^-$.

2.9. Calculation of NH$_3$ selectivity

The NH$_3$ selectivity is calculated as follows:

$$Selectivity = \frac{c_{NH_3}}{\Delta c_{NO_3^-}} \times 100\%$$

Where c_{NH_3} is the measured NH$_3$ concentration, and $\Delta c_{NO_3^-}$ is the concentration difference of NO$_3^-$ before and after electrolysis.

2.10. The reaction apparent activation energy tests

To determine the apparent activation energy (E_a) associated with the NO$_3$RR, the catalysts electrochemical measurements were carried out in 1 M KOH solution containing 0.1 M KNO$_3$ at various temperatures. In the context of heterogeneous electrocatalytic reactions, the current density can be correlated with E_a using the Arrhenius equations [38,39].

$$j = A_a \exp(-\frac{E_a}{RT})$$

where A_a represents the apparent pre-exponential factor, R stands for the ideal gas constant (8.314 J·K·mol^{-1}), T denotes the temperature in Kelvin (K). Hence, E_a can be determined further by fitting the slope of the Arrhenius plot using the following equations.

$$\left| \frac{\partial(\log_{10}j)}{\partial 1/T} \right|_\eta = -\frac{E_a}{2.303R}$$

the intercept of $\log_{10} j$ *vs.* $1/T$ plot corresponds to the logarithm of A_a.

2.11. K^{15}NO$_3$ isotope labeling experiments

The isotope labeling experiment was conducted in a 1 M KOH solution containing 0.1 M K^{15}NO$_3$ (98% ^{15}N atom) through chronoamperometry measurements for 1 h at —0.15 V *vs.* RHE. In brief, the pH of the treated electrolyte was adjusted to 3 using a 4 M H$_2$SO$_4$ solution. Subsequently, added electrolyte (400 μL) and deuterium oxide (D$_2$O) (150 μL) into the NMR tube, with the subsequent detection of ^{15}NH$_4^+$ in the electrolyte using 1 H NMR (500 MHz).
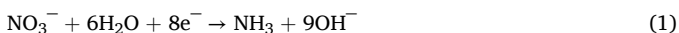
2.12. In situ FTIR spectroscopy

FTIR measurements were conducted using an IRTracer-100 spectrometer. The electrochemical cell was constructed on top of a CaF$_2$ prism, with the electrode positioned against it to create a thin layer. The measurements were conducted using external reflection. The electrochemical cell was assembled in a three-electrode configuration, comprising a Pt wire counter electrode, an Ag/AgCl (saturated KCl) reference electrode, and a working electrode created by depositing a 20 μL ink of electrocatalyst onto a gold (Au) sheet. The electrolyte used was Ar-saturated 1 M KOH with 0.1 M NO$_3^-$. FTIR spectra were collected by averaging 512 scans with a resolution of 8 cm^{-1} at specific potentials. The potentiostatic model is employed, with potentials scanned ranging from 0.25 V to −0.35 V *vs.* RHE, in comparison to the reference potential of 0.25 V *vs.* RHE. The spectra were expressed as −lg (R/R$_0$), where R represents the reflectance at a set potential, and R$_0$

denotes the reflectance at the reference potential. Hence, positive bands in the ratio indicate the formation of species at the sample potential, while negative bands correspond to the depletion of species at the sample potential.

2.13. DFT Calculations

Utilizing the Vienna ab initio Simulation Package (VASP) [40,41], spin-polarized density functional theory (DFT) calculations were executed to characterize electron-ion interactions and assess exchange-correlation energies, respectively, by employing the projector-augmented wave (PAW) [42,43] potentials coupled with the Perdew-Burke-Ernzerhof (PBE) [44] functional on the basis of the generalized gradient approximation (GGA). The Monkhorst-Pack grids of $3 \times 6 \times 1$ and $3 \times 3 \times 1$ k-points were used for geometric optimizations of the Ag(111) and Ni-Ni(OH)$_2$ slabs, respectively, with a convergence threshold set at 10^{-5} eV for energy and 0.02 eV Å^{-1} for force, along with a cutoff of 520 eV for the plane wave basis set. The representative slabs were consisted of 4 layers where the bottom two layers were fixed while the remaining two with the adsorbates were fully relaxed without constraints. Vacuum spaces greater than 20 Å were incorporated along the nonperiodic directions to minimize any spurious interactions between neighboring slabs.

Under standard circumstances, the NO$_3$RR reaction can be elucidated by eq1:

$$NO_3^- + 6H_2O + 8e^- \rightarrow NH_3 + 9OH^- \tag{1}$$

These calculations addressed the derivation of the charged nitrate anion in the solvent and its initial adsorption onto the catalyst surface, which was accomplished by considering the process NO$_3^-$ (l) → HNO$_{3(l)}$ → HNO$_{3(g)}$ → *NO$_3$[45]. Additionally, the Gibbs free energy change arising from the gas-liquid state of the individual intermediates was taken into account. The Gibbs free energy of NO$_3$ adsorption in the initial step is computed using eq2:

$$\Delta G_{*NO3} = G*NO_3 + 1/2G_{H2} - E* - G_{HNO3(g)} + 0.392 \text{ eV} \tag{2}$$

Note that $G*NO_3 = E*NO_3 - T\Delta S$, where only the vibrational entropy was taken into consideration. Subsequently, all gas-phase Gibbs free energies were calculated according to eq3:

$$\Delta G = \Delta E + \Delta ZPE - T\Delta S + \Delta G_U + \Delta G_{pH} \tag{3}$$

Here, ΔE represented the total energy of the surface slab, while ΔZPE [46] and ΔS denoted the calculated zero-point energy correction and entropy, respectively. These values were derived from vibrational frequency calculations of the adsorbed species, encompassing the translational, vibrational, and rotational modes. The entropies (ΔS) of the gas-phase NH$_3$, H$_2$, and H$_2$O were obtained as referenced [47–50]. Meanwhile, the entropy of H$_2$O was computed at 0.035 bar, the equilibrium pressure atwhich the free energy of gas-phase water matches that of liquid water at room temperature.

Note that the electronic energy and Gibbs free energy of OH$^-$ were estimated according to the reference in eq4 [51]:

$$E(OH^-) = E(H_2O) - 1/2E(H_2), G(OH^-) = G(H_2O) - 1/2 G(H_2) \tag{4}$$

where the reversible hydrogen electrode (RHE) [51] served as the electrochemical reference.

The effect of the applied external electrode potential on free energy was computed utilizing eq5:

$$\Delta G_U = - eU \tag{5}$$

Here, e represents the charge of the system, and U denotes the operating potential applied relative to the Reversible Hydrogen Electrode (RHE).

Considering the impact of the solution pH in the experiment, the free energies were accordingly adjusted based on the H$^+$ concentration in the solution using eq6 [12]:

$$\Delta G_{pH} = - K_BTln[H^+] = K_BTln10*pH \tag{6}$$

Here, K_B represents Boltzmann's constant, and T denotes the temperature.

3. Results and discussion

3.1. Characterization of Catalyst Structure and Morphology

The schematic illustration of Ag@Ni/Ni(OH)$_2$ NWs synthesis is presented in Fig. 1**a**. Initially, Ag NWs were synthesized using the polyol reduction method[33,34]. Fig. 1**b** and Figures S2 illustrate that the resulting Ag NWs, featuring an average diameter of 173.24 nm and an average length of 21.43 μm, exhibit a smooth and clean surface. Energy dispersive X-ray spectrometers (EDS) elemental mapping images demonstrate the even distribution of Ag throughout the Ag NWs (Figure S3). The high-resolution transmission electron microscopy (HRTEM) image reveals lattice fringe distances of 0.24 and 0.202 nm (Fig. 1**c**), indicative of the (111) and (200) planes of Ag-NWs [52].

Following synthesis, the Ag NWs were dispersed in a 10 mL oleylamine solution containing 30 mM Ni(OAc)$_2$·4 H$_2$O. The mixture underwent heating at 200 ℃ for 1 hour under vigorous stirring in an argon atmosphere. The synthesized Ag@Ni/Ni(OH)$_2$ NWs exhibit an average diameter of 200.14 nm and an average length of 22.49 μm (Figure S4). The scanning electron microscopy (SEM) image verified a rough layer composed of numerous nanoparticles is formed on the Ag NWs surface (Fig. 1**d**). The HRTEM image of the nanoparticles reveals distinct lattice fringes with a measured distance of 0.212 nm and 0.232/0.284 nm (Fig. 1**e**), corresponding to the (111) plane of Ni and (101)/(100) plane of Ni(OH)$_2$, respectively[24,32,53]. HRTEM analysis indicated that the nanoparticles on the Ag NWs surface consisted of connected Ni (0) and Ni(OH)$_2$. The conclusion that Ni and Ni(OH)$_2$ co-exist in nanoparticles can be further proved by X-ray photoelectron spectroscopy (XPS) studies. As shown in Fig. 1**h**, the Ni 2p$_{3/2}$ peaks at 852.8 and 855.3 eV attributed to the Ni (0) and Ni-OH are observed [24,54].

Energy dispersive X-ray spectrometers (EDX) line profile verify the Ag@Ni/Ni(OH)$_2$ NWs exhibit a core-shell structure with Ag core and Ni shell (Fig. 1**i**). This core-shell structure will shield the Ag active sites and reduce the conversion efficiency for NO$_3^-$ to NO$_2^-$. The synergy between the Ag and Ni phases will also be limited due to the lack of atomic-level Ag/Ni interfaces. To cover these shortages, we activated the Ag@Ni/Ni(OH)$_2$ NWs (labeled as A-Ag@Ni/Ni(OH)$_2$ NWs) in 0.1 M KNO$_3$ + 1 M KOH solution for 1 h at a high reduction bias (-1.05 V *vs*. RHE). The electrochemical activation process has no effect on the length of the A-Ag@Ni/Ni(OH)$_2$ NWs (Figure S5), but it contributes to a smoother surface when compared to the Ag@Ni/Ni(OH)$_2$ NWs (Fig. 1**f**). The HRTEM image (Fig. 1**g**) demonstrate that the Ni-phase still maintains the Ni/Ni(OH)$_2$ heterostructure after electrochemical treatment. Moreover, the XPS spectrum (Fig. 1**h**) reveals that the peak ratio of Ni(0) to Ni (2+) decreases after electrochemical treatment, suggesting that a portion of Ni(0) converts to Ni(2+) during the electrochemical process. Drawing on explanations gleaned from the literature [25,55,56], the following mechanism is proposed for formation of Ni^{2+} from the Ni(0) under a negative cathode potential. During cathodic NO$_3$RR alongside HER, a highly alkaline layer forms on the electrode surface, abundant in alkali cations such as K$^+$, resembling a molten alkali salt. Under cathodic polarization, Ni metal accepts electrons, transitioning to its anionic form (Ni^{x-}) [55,56]. The Ni^{x-} are stabilized by K$^+$, forming negatively charged ions known as "Zintl ions" (Ni^{x-}, K$^+$) [55,57]. These ions are transient and reactive, undergoing subsequent oxidation by H$_2$O to produce charge-neutral Ni atoms, which then aggregate to form metallic nanoparticles deposited on the cathode surface [58]. The nano-sized Ni exhibits high activity ($E_{Ni^{2+}}$ = -0.257 V) and can undergo further
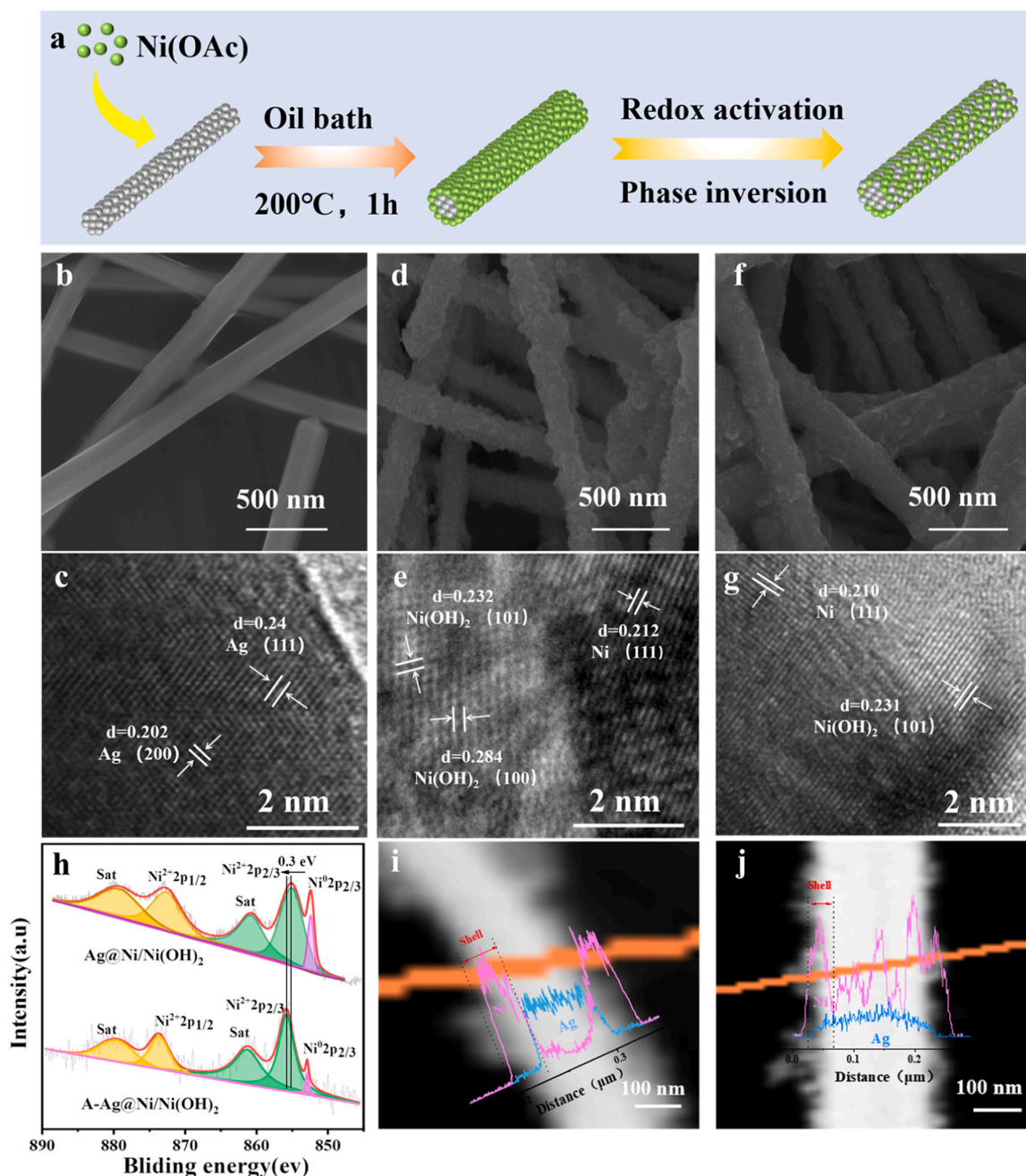
Fig. 1. (a) Schematic illustration of the synthetic process of the A-Ag@Ni/Ni(OH)$_2$ NWs catalyst. SEM images of (b) Ag NWs, (d) Ag@Ni/Ni(OH)$_2$ NWs, and (f) A-Ag@Ni/Ni(OH)$_2$ NWs. HRTEM image of (c) Ag NWs, (e) Ag@Ni/Ni(OH)$_2$ NWs, and (g) A-Ag@Ni/Ni(OH)$_2$ NWs. (h) XPS spectra of Ni 2p of the Ag@Ni/Ni(OH)$_2$ NWs and A-Ag@Ni/Ni(OH)$_2$ NWs. (i) EDX line−scan of a selected area Ag@Ni/Ni(OH)$_2$ NWs and (j) A-Ag@Ni/Ni(OH)$_2$ NWs.

oxidation by oxygen dissolved in the solution ($E_{O_2/OH^-} = 0.806$ V, pH = 7), resulting in the formation of Ni(OH)$_2$. These results suggest that Ni (OH)$_2$ can remain stable throughout the electrochemical activation process and further supported by the Raman spectra (Figure S6). Following electrochemical treatment, the Raman peak corresponding to the typical Raman activity mode at 517 cm^{-1} in Ni(OH)$_2$ is still preserved. Simultaneously, we utilized XPS to further analyze the impact of electrochemical activation treatment on the valence of other elements on the catalyst surface. As shown in Figure S7, the XPS spectra obtained over a wide scan range of the prepared catalysts reveal prominent peaks corresponding to C 1 s, O 1 s, Ni 2p, and Ag 3d, indicating their strong presence. The carbon element primarily originates from the conductive adhesive utilized during the XPS testing procedure. The oxygen element present on the Ag NWs surface primarily derives from the residual

polyvinylpyrrolidone (PVP) ligands adhering to its surface. Serving as both a stabilizer and a crystal structure guiding agent, PVP plays a pivotal role in the successful synthesis of silver nanowires [33,34]. To ascertain the source and valence state of the oxygen element in Ag@Ni/Ni(OH)$_2$ NWs and A-Ag@Ni/Ni(OH)$_2$ NWs, we conducted an analysis of the high-resolution XPS spectrum of the oxygen element. As shown in Figure S8, the high resolution O 1 s spectrum can be deconvoluted into three major species: lattice O in metal oxides at 529.4 eV, hydroxide O (Ni-O-H) at 530.9 eV, and chemisorbed O at 532.2 eV. Clearly, hydroxide O (Ni-O-H) becomes dominant after electrochemical treatment, aligning with the observed trend in the XPS signal change of Ni^{2+}. The high-resolution XPS spectra for the Ag show that the Ag 3d$_{5/2}$ peak appeared at a binding energy of 367.6 eV, and the splitting of the 3d doublet was 6.0 eV. This binding energy indicated that silver retains

metallic nature during electrochemical activation process [59].

EDX line profile showed that Ag atoms migrate outward to the surface of nanowires, which resulted in the exposure of Ag active sites (Fig. 1**j**). The X-ray photoelectron spectroscopy (XPS) studies on the prepared catalysts further validate this migration process (Figure S8). The XPS spectrum of Ag NWs shows a strong peak at 367.8 and 373.8 eV belonging to Ag 3d. However, the XPS spectrum of Ag@Ni/Ni(OH)$_2$ NWs exhibits a fragile Ag 3d signal because the Ag core is predominantly enveloped by the Ni/Ni(OH)$_2$ shell. In contrast, after electrochemical activation treatment, the XPS signal for Ag 3d was re-enhanced in the XPS spectrum of A-Ag@Ni/Ni(OH)$_2$ NWs. The migration of Ag atoms outward to the surface of the NWs can attribute to Ag more potent binding energies with NO$_3^-$ [18,60]. Choi C. also found a similar result during the Cu/Ag interface construction [61]. EDS elemental mapping image demonstrates the outmigration of Ag core leading to the formation of atomic Ag-Ni interfaces on the surface of A-Ag@Ni/Ni(OH)$_2$ NWs (Figure S9). The XPS spectra reveal that the electron binding energy of Ni shifted positively by 0.3 eV after Ag migration to the surface (Fig. 1**h**), while that of Ag shifted negatively by 0.27 eV (Figure S8), suggesting electron transfer from Ni to Ag upon activation. The XRD patterns of the prepared catalysts exhibit the position and half-peak

width of the Ag diffraction peak in A-Ag@Ni/Ni(OH)$_2$ and Ag@Ni/Ni(OH)$_2$ catalysts show almost no difference (Figure S10). This result indicates that the lattice spacing of Ag remains unchanged after being combined with Ni/Ni(OH)$_2$, suggesting the absence of lattice stress between the Ag phase and the Ni-based phase. These structural improvements will be more conducive to the conversion of NO$_3^-$ to NO$_2^-$, as well as the synergy between the Ag and Ni phases, as discussed below.

3.2. Eelectrocatalytic performance of the catalyst

The electrocatalytic activity of the as-synthesized catalysts for NO$_3$RR was assessed in a 1 M KOH and 0.1 M NO$_3^-$ solution. The linear sweep voltammetry (LSV) curve of A-Ag@Ni/Ni(OH)$_2$ NWs reveals the highest current density among the as-synthesized catalysts (Fig. 2**a**). This signifies that the catalytic activity of A-Ag@Ni/Ni(OH)$_2$ NWs in NO$_3$RR outperforms that of Ag NWs and Ag@Ni/Ni(OH)$_2$ NWs. Moreover, A-Ag@Ni/Ni(OH)$_2$ NWs exhibit a higher double-layer capacitance (Cdl) value of 1.01 mF cm^{-2} compared to Ag@Ni/Ni(OH)$_2$ NWs (0.752 mF cm^{-2}) and Ag NWs (0.383 mF cm^{-2}) (Fig. 2**b**), suggesting A-Ag@Ni/Ni(OH)$_2$ NWs have a higher electrochemically active surface area (ECSA) for NO$_3$RR [62]. Electrochemical impedance spectroscopy
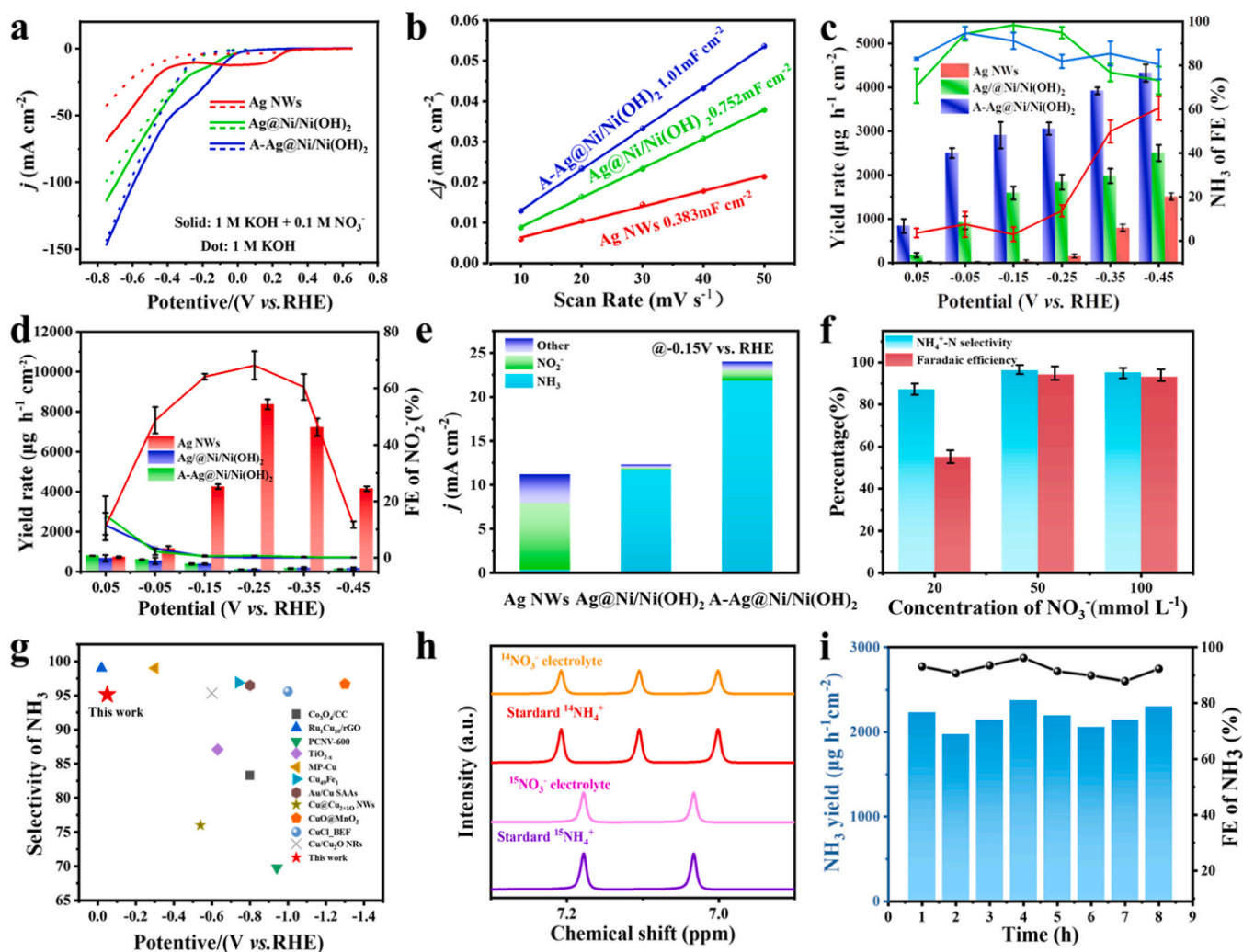

Fig. 2. NO$_3^-$ -to- NH$_3$ conversion performance. (a) LSV curves of the as-synthesized catalysts in 1 M KOH electrolyte with and without KNO$_3$. (b) The determination of double-layer capacitance for each catalyst. (c) NH$_3$ yields and FEs, (d) NO$_2^-$ yields and FEs of Ag NWs, Ag@ Ni/Ni(OH)$_2$ NWs, and A-Ag@Ni/Ni(OH)$_2$ NWs. (e) The current densities of NH$_3$, NO$_2^-$, and other products were collected at −0.15 V *vs.* RHE. (f) Effects of initial NO$_3^-$ concentration on NH$_4^+$ selectivity and FE. (g) Comparison of NH$_4^+$ selectivity on the A-Ag@Ni/Ni(OH)$_2$ NWs with other extensively reported electrocatalysts. (h) ^{1}HNMR spectra of ^{15}NH$_4$Cl and ^{14}NH$_4$Cl standard solutions and electrolyte after the NO$_3$RR electrolysis using K^{15}NO$_3$ and K^{14}NO$_3$ as the nitrogen source. (i) Stability test of A-Ag@Ni/Ni(OH)$_2$ NWs at −0.05 V *vs.* RHE.

(EIS) measurements demonstrated that A-Ag@Ni/Ni(OH)$_2$ NWs exhibit the smallest charge-transfer resistance (R_{ct}) (Figure S12), signifying accelerated electron transfer and enhanced kinetics in adsorbed reactants (intermediates) during NO$_3$RR, particularly in comparison to Ag@Ni/Ni(OH)$_2$ NWs [63].

The yield rates and Faradaic efficiencies (FEs) for the products (NH$_3$ and NO$_2^-$) of the as-synthesized catalysts were examined in the 1 M KOH + 0.1 M KNO$_3$ solution at varying applied potentials (Fig. 2c, d). The resulting products were quantified through ultraviolet-visible (UV–Vis) spectrophotometry. (Figures S13, S14). As shown in Fig. 2c, the NH$_3$ yield rate and FEs of A-Ag@Ni/Ni(OH)$_2$ NWs are obviously improved compared with Ag@Ni/Ni(OH)$_2$ NWs and Ag NWs resulting in the synergy between the Ag and Ni phases. The NH$_3$ yield rate of A-Ag@Ni/Ni(OH)$_2$ NWs increases with the applied potential negative moving, reaching a value of 4354.67 µg h^{-1} cm^{-2} at —0.45 V vs. RHE, whereas FEs values hit a maximum of 94.78% at —0.15 V vs. RHE. The slight deterioration of FEs at more negative potentials could be ascribed to the competing HER. Figure S15 shows that the pH changed negligibly during the catalytic NO$_3$RR process of A-Ag@Ni/Ni(OH)$_2$ NWs at —0.05 V vs. RHE, indicating the that fluctuations in NO$_3^-$ or NO$_2^-$ concentration have little effect on the pH value of the electrolyte. Although the FEs of Ag@Ni/Ni(OH)$_2$ NWs are similar to A-Ag@Ni/Ni(OH)$_2$ NWs, however, the NH$_3$ yield rate is much lower due to the Ag active sites shielded by Ni/Ni(OH)$_2$ shell, only 2500.1 µg h^{-1} cm^{-2} at —0.45 V vs. RHE. We synthesized Ni/Ni(OH)$_2$ and assessed its catalytic activity in NO$_3$RR, providing further evidence that the synergistic interaction between the Ag phase and Ni-based phase enhances NO$_3^-$ reduction to NH$_3$. As shown in Figure S16a, the high-resolution XPS spectra for the Ni 2p indicate that the valence states of Ni in Ni/Ni(OH)$_2$ are 0 and 2+. Further confirmation of the presence of divalent Ni as Ni(OH)$_2$ comes from the Raman spectrum (Figure S16b). Figures S16c-d compare the catalytic activity of Ni/Ni(OH)$_2$ and A-Ag@Ni/Ni(OH)$_2$ NWs for NO$_3$RR. Clearly, the catalytic activity of Ni/Ni(OH)$_2$ for NO$_3$RR is significantly lower than that of A-Ag@Ni/Ni(OH)$_2$ NWs, primarily due to the absence of Ag's synergistic effect. The Ag NWs catalyzes the conversion of NO$_3^-$ to NH$_3$ only at < —0.25 V vs. RHE. Its NH$_3$ yield rate and FEs are 1498.5 µg h^{-1} cm^{-2} and 49.88% at —0.45 V vs. RHE, respectively, significantly lower than A-Ag@Ni/Ni(OH)$_2$ NWs. Fig. 2d shows the Ag NWs have the highest NO$_2^-$ yield rate of 8470.02 µg h^{-1} cm^{-2} and FEs of 72.4% at —0.25 V vs. RHE. These results indicate Ag NWs exclusively efficiently catalyze the formation of NO$_2^-$ at > —0.25 V vs. RHE, and catalyze the conversion of NO$_2^-$ to NH$_3$ at < —0.25 V vs. RHE with low efficiency. Since the Ni-based phases of Ag@Ni/Ni(OH)$_2$ NWs and A-Ag@Ni/Ni(OH)$_2$ NWs can efficiently catalyze NO$_2^-$ reduction to NH$_3$, virtually no NO$_2^-$ was detected throughout the entire test potential range. These conclusions definitively establish that the synergistic effect of the Ag phase and Ni-based phase confers A-Ag@Ni/Ni(OH)$_2$ NWs with superior catalytic activity for NO$_3$RR. This outstanding catalytic performance is primarily attributable to the A-Ag@Ni/Ni(OH)$_2$ NWs themselves, rather than the carbon paper used as a support (Figure S17).

The disparity in the LSV of A-Ag@Ni/Ni(OH)$_2$ NWs between the absence and presence of NO$_3^-$ is negligible (Fig. 2a), implying that the catalytic performance of A-Ag@Ni/Ni(OH)$_2$ NWs for HER and NO$_3$RR is closely comparable. However, the FEs of A-Ag@Ni/Ni(OH)$_2$ NWs for NO$_3$RR is as high as 85.37% even at —0.45 V vs. RHE (Fig. 2c), proving that HER is limited in the presence of nitrate. Based on this conclusion, we preliminary speculate that the NO$_3$RR on A-Ag@Ni/Ni(OH)$_2$ NWs follows the H$_{ads}$-mediated pathway. Namely, the H$_{ads}$ generated by the Ni-based phase preferentially reduce the absorbed NO$_3^-$ to NH$_3$, leading to the Heyrovsky (H$_{ads}$ + H$_3$O$^+$ + e$^-$ → H$_2$ + H$_2$O) step of HER being limited. In addition, The NH$_3$ yield rate of A-Ag@Ni/Ni(OH)$_2$ NWs did not increase significantly with the negative shift of the potential, especially in the potential range from —0.05 to —0.25 V vs. RHE, the NH$_3$ yield rate only slightly increased of 20%. However, the previous reports suggest that the NH$_3$ yield rate of catalysts based on the electron

reduction pathway, such as Cu-RD, Py-Ag NSs, ox-LIG, are dramatically enlarged at more negative potential [64–66]. For the H$_{ads}$-mediated pathway, it is well understood that the NH$_3$ yield rate is highly correlated with the amounts of H$_{ads}$ rather than the electron density on the electrode surface. Given the outstanding catalytic performance of Ni/Ni(OH)$_2$ in the HER, the H$_{ads}$ generated on the catalyst surface can tend to be saturated at low potentials. As a result, the NH$_3$ yield rate of A-Ag@Ni/Ni(OH)$_2$ NWs exhibits low sensitivity to changes in potential. Although Ag@Ni/Ni(OH)$_2$ NWs also have excellent catalytic performance for HER, the active sites of Ag are shielded by the Ni/Ni(OH)$_2$ phase, resulting in a deficiency of active sites for adsorbing NO$_3^-$ on the catalyst surface, so its NH$_3$ yield rate is far lower than that of A-Ag@Ni/Ni(OH)$_2$ NWs. This further underscores the significance of the synergy between the Ag-based phase and Ni-based phase in the process of NO$_3$RR.

Fig. 2e shows the selectivity of A-Ag@Ni/Ni(OH)$_2$ NWs for synthesizing NH$_3$. The A-Ag@Ni/Ni(OH)$_2$ NWs attained the highest partial current density for synthesizing NH$_3$ (21.84 mA cm^{-2}) and lowest partial current density for all by-products (< 3 mA cm^{-2}) at –0.15 V vs. RHE. This suggests that A-Ag@Ni/Ni(OH)$_2$ NWs can achieve more efficient NH$_3$ synthesis. Fig. 2f shows the selectivity of A-Ag@Ni/Ni(OH)$_2$ NWs for synthesizing NH$_3$ at −0.05 V vs. RHE under various nitrate concentrations. It was apparent that the high NO$_3^-$-to-NH$_3$ selectivity achieved on A-Ag@Ni/Ni(OH)$_2$ NWs at a wide range of NO$_3^-$ concentrations (from 20 to 100 mM), and NH$_4^+$ selectivity surpasses 96.12% at concentrations exceeding 50 mM. The decline in FE observed at 20 mM is ascribed to the diminished diffusion rate of NO$_3^-$ in the electrolyte liquid phase toward the electrode surface, resulting in sluggish electrode reaction kinetics. In contrast, the competitive reaction becomes more pronounced, resulting in a decrease in faradaic efficiency [67]. Impressively, The NH$_4^+$ selectivity of the NO$_3$RR on A-Ag@Ni/Ni(OH)$_2$ NWs exceeding that of the majority of other electrocatalytic NO$_3$RR work (Fig. 2g and Table S1)[63,67–76].

Control experiments were conducted to verify that the generated NH$_3$ originates specifically from the reduction of NO$_3^-$ on A-Ag@Ni/Ni(OH)$_2$ NWs. As shown in Figure S18, the NH$_3$ yield rate of A-Ag@Ni/Ni(OH)$_2$ NWs without NO$_3^-$ was found to be negligible (< 20 µg h^{-1} cm^{-2}). Additionally, an isotope tracing experiment using ^{15}NO$_3^-$ as the reactant was performed. As depicted in the ^{1}H nuclear magnetic resonance (HNMR) spectra (Fig. 2h), the ^{15}NH$_3$ generated using ^{15}NO$_3^-$ exhibited two peaks, whereas ^{14}NH$_3$ from ^{14}NO$_3^-$ displayed three peaks [77]. The aforementioned results collectively demonstrate that the NH$_3$ was derived exclusively from the NO$_3$RR, ruling out contributions from other impurities. Electrochemical stability was assessed by replacing the electrolyte every hour for 8 cycles at −0.05 V vs. RHE. Fig. 2i illustrates no significant alteration in NH$_3$ production and FE of A-Ag@Ni/Ni(OH)$_2$ NWs during prolonged electrolysis. The LSV curves for A-Ag@Ni/Ni(OH)$_2$ NWs remain virtually identical before and after stability testing (Figure S19).

3.3. Research on synergistic effect of Ag and Ni phases

To further understand the synergy between the Ag and Ni phases in A-Ag@Ni/Ni(OH)$_2$ NWs for catalytic NO$_3$RR. The overpotential at −10 mA·cm^{-2} and the Tafel slope were determined from the LSV curves of the as-synthesized catalysts in 0.1 M NO$_3^-$ and NO$_2^-$, respectively (Figure S20). As depicted in Fig. 3a-c, Ag NWs exhibit the most positive potential (0.18 V vs. RHE) for NO$_3^-$ reduction, confirming the lowest energy barrier for NO$_3^-$ reduction. The corresponding Tafel slope is 120 mV dec^{-1}, suggesting that the rate-determining step (RDS) is the initial one-electron transfer occurring during the NO$_3^-$ to NO$_2^-$ conversion [78,79]. In the case of core-shell Ag@Ni/Ni(OH)$_2$ NWs, the overpotential for NO$_3^-$ reduction shifts negatively to —0.11 V vs. RHE due to the Ag core being covered by the Ni/Ni(OH)$_2$ shell, indicating an increased energy barrier for NO$_3^-$ reduction. The significantly higher Tafel slope of Ag@Ni/Ni(OH)$_2$ NWs (198 mV dec^{-1}) suggests that the
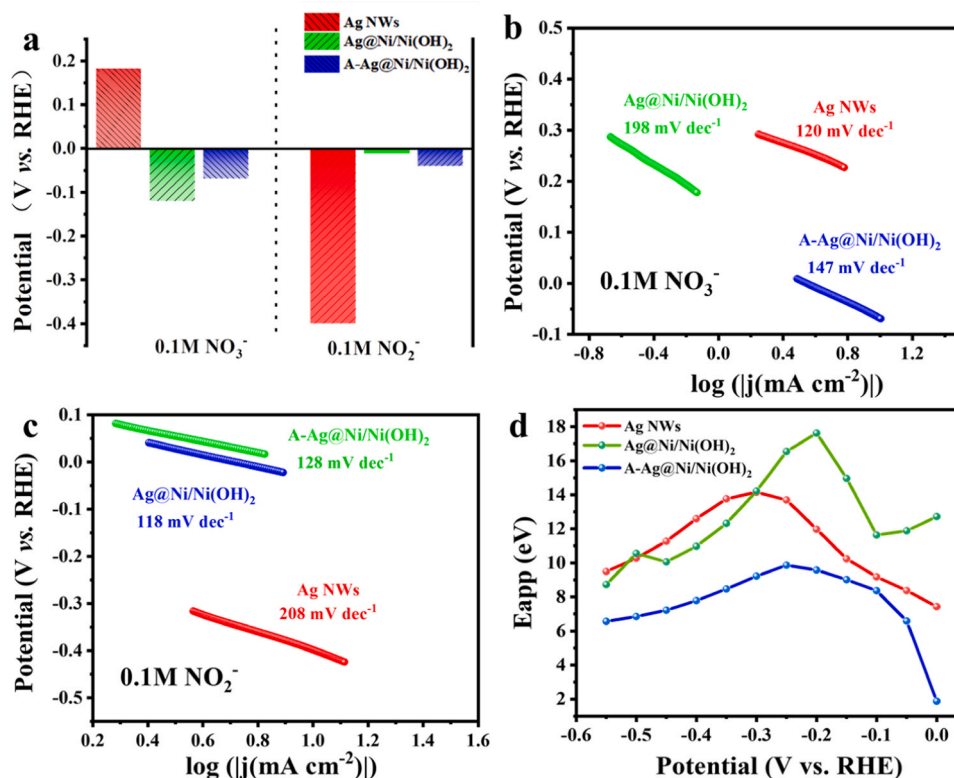
Fig. 3. (a) The LSV-derived potentials at a current density of -10 mA cm^{-2} for NO$_3^-$ and NO$_2^-$ reduction on Ag NWs, Ag@Ni/Ni(OH)$_2$ NWs, A-Ag@Ni/Ni(OH)$_2$ NWs catalysts. The LSV-derived Tafel slopes of Ag NWs, Ag@Ni/Ni(OH)$_2$ NWs, A-Ag@Ni/Ni(OH)$_2$ NWs, and in (b) 0.1 M NO$_3^-$ (c) 0.1 M NO$_2^-$ at pH =14, respectively. (d) Ag NWs, Ag@Ni/Ni(OH)$_2$ NWs, and A-Ag@Ni/Ni(OH)$_2$ NWs catalyzed the activation energy for the NO$_3$RR at various potentials.

initial adsorption and activation of NO$_3^-$ limit the NO$_3$RR process [78]. Following electrochemical activation treatment, the overpotential of A-Ag@Ni/Ni(OH)$_2$ NWs for NO$_3^-$ reduction shifts to —0.06 V *vs*. RHE, and the Tafel slope decreases to 147 mV dec^{-1}, indicating enhanced catalytic performance for NO$_3^-$ reduction. The improved catalytic activity of A-Ag@Ni/Ni(OH)$_2$ NWs for NO$_3^-$ reduction is attributed to the outward migration of Ag atoms.

For the reduction of NO$_2^-$, Ag NWs demonstrate the most negative potential (—0.40 V *vs*. RHE) (Fig. 3**a**), indicative of the highest energy barrier for the catalytic reduction of NO$_2^-$ to NH$_3$. The elevated Tafel slope (208 mV dec^{-1}) implies that the highest energy barrier primarily originates from the lower capacity of Ag NWs for NO$_2^-$ absorption [26, 79]. In contrast, the overpotential of Ag@Ni/Ni(OH)$_2$ NWs shifts to -0.01 V *vs*. RHE, accompanied by a decrease in the corresponding Tafel slope to 118 mV dec^{-1}. This indicates that the Ni/Ni(OH)$_2$ shell presents a lower energy barrier and higher kinetic rate for the catalytic reduction of NO$_2^-$. Following electrochemical activation treatment, the overpotential (-0.03 V *vs*. RHE) and Tafel slope (128 mV dec^{-1}) of NO$_2^-$ reduction on the A-Ag@Ni/Ni(OH)$_2$ NWs closely resemble those of the Ag@Ni/Ni(OH)$_2$ NWs. This result suggests that the electrochemical activation process has no negative impact on the catalytic performance of Ni/Ni(OH)$_2$ shell for NO$_2^-$ reduction. As a result, we can conclude that NO$_3^-$ is reduced to NO$_2^-$ preferentially on Ag phases, while the subsequent conversion of NO$_2^-$ to NH$_3$ is down to the Ni-based phase.

Based on the synergistic effect between Ag phase and Ni-based phase, it can be seen that regulating the ratio of Ag and Ni on the catalyst surface is pivotal for maximizing catalytic activity. Given that the ratio of Ag to Ni on the catalyst surface can be regulated by adjusting the activation time, we conducted electrochemical activation of the Ag@Ni/Ni(OH)$_2$ NWs catalyst for various durations. Subsequently, we evaluated the catalytic activity of A-Ag@Ni/Ni(OH)$_2$ NWs for the NO$_3$RR at a potential of —0.05 V *vs*. RHE. As depicted in Figure S21a, the catalytic activity of A-Ag@Ni/Ni(OH)$_2$ NWs for the NO$_3$RR have peaked

following a 1-hour activation period. Subsequently, XPS was employed to scrutinize the surface composition of the Ag@Ni/Ni(OH)$_2$ NWs catalyst both pre and post 1-hour activation. The findings revealed an escalation in Ag content on the catalyst surface from 2.15% to 27.84% subsequent to activation (Figure S21b). Combining the catalytic activity results, we infer that the optimal Ag to Ni ratio on the catalyst surface is 1:2.6. If the activation time be further extended, we anticipate a corresponding increase in the Ag content on the catalyst surface, potentially leading to adverse effects on NO$_3$RR catalysis.

We performed a temperature-dependent kinetic analysis of the synthesized catalyst to ascertain the activation energy (E_a) of the NO$_3$RR process (Figure S22). The resulting E_a shows a high energy barrier of 14.12 kJ mol^{-1} at -0.3 V *vs*. RHE for Ag NWs (Fig. 3**d**). The potential corresponding to the energy barrier is consistent with the overpotential of reducing NO$_2^-$ (—0.30 V *vs*. RHE). In addition, Fig. 2**c** and **d** reveal that the Ag NWs initiated the catalytic conversion of NO$_2^-$ to NH$_3$ at —0.25 V *vs*. RHE. These results indicate the RDS of NO$_3$RR on the Ag NWs is the catalytic conversion of NO$_2^-$ to NH$_3$. For the Ag@Ni/Ni(OH)$_2$ NWs, the corresponding E_a shows a high energy barrier of 17.4 kJ mol^{-1} at —0.15 V *vs*. RHE (close to the overpotential of reducing NO$_3^-$), indicating the RDS of NO$_3$RR on the Ag@Ni/Ni(OH)$_2$ NWs is the catalytic reduction of NO$_3^-$ to NO$_2^-$. Contrastingly, post-electrochemical activation treatment, the energy barrier at -0.15 and -0.3 V *vs*. RHE experiences a significant reduction. This reduction indicates an accelerated overall kinetic rate of the NO$_3$RR on the A-Ag@Ni/Ni(OH)$_2$ NWs, attributable to the synergistic interaction between the Ag and Ni phases.

3.4. Research on the mechanism of NO$_3$RR promotion by the Ni/Ni(OH)$_2$ phase

For the NO$_3$RR via the H$_{ads}$-mediated pathway, the H$_{ads}$ plays an important role in each step, particularly the hydrogenation step. To investigate the promoting effect of H$_{ads}$ in NO$_3$RR, we measured cyclic

voltammogram (CV) curves of the catalyst in a 1 M KOH solution with or without KNO$_3$ utilizing a low scanning rate (2 mV/s). As reported previously, the area of the hydrogen characteristic peak at 0.43 V is proportional to the H$_{ads}$ enrichment on the catalyst surface [80]. As shown in Figure S24, a peak at 0.43 V *vs.* RHE emergenced in the CV curves of A-Ag@Ni/Ni(OH)$_2$ NWs, indicating the generation of H$_{ads}$ on the A-Ag@Ni/Ni(OH)$_2$ NWs surface. Moreover, the hydrogen peak area decreases obviously after the addition of NO$_3^-$, thereby confirming that NO$_3^-$ promotes H$_{ads}$ consumption.

To verify the Ni/Ni(OH)$_2$ phase catalyzes the NO$_3$RR via the H$_{ads}$-mediated pathway. Tert-butyl alcohol (TBA) was used to assess the involvement of atomic H$_{ads}$ in NO$_3$RR. TBA can react with H$_{ads}$ on the catalyst surface, yielding hydroxyl radicals (OH·) and butene radicals (C$_4$H$_9$·). The resulting OH· can further react with another H$_{ads}$ to form H$_2$O. Therefore, TBA, as a quencher for H$_{ads}$, can effectively reduce the concentration of H$_{ads}$ on the catalyst surface and is widely utilized to study the promotional effect of H$_{ads}$ on NO$_3$RR [67]. In Fig. 4a, the negligible change in overpotential for NO$_3^-$ reduction upon the addition of TBA to the Ag NWs cathode indicates that the reduction of NO$_3^-$ on the Ag NWs primarily follows an electron reduction pathway. In contrast, as for Ag@Ni/Ni(OH)$_2$ NWs and A-Ag@Ni/Ni(OH)$_2$ NWs cathode, the impact of TBA on NO$_3$RR decay kinetics was more evident, the overpotential for NO$_3^-$ reduction shifted negatively by −0.15 and −0.1 V *vs.* RHE after adding TBA, respectively. Fig. 4b presents the chronoamperometry curve of as-synthesized catalysts in 1.0 M KOH + 0.1 M KNO$_3$ before and after adding 1 mM TBA. Obviously, for the Ag NWs, the negligible cathode current change was observed upon the addition of TBA. In contrast, the cathode current of NO$_3$RR on the Ag@Ni/Ni(OH)$_2$ NWs and A-Ag@Ni/Ni(OH)$_2$ NWs dropped sharply after adding 1 mM TBA.

The influence of TBA on the NH$_3$ yield rate and Faradaic efficiencies (FEs) of A-Ag@Ni/Ni(OH)$_2$ NWs are further examined. As depicted in Fig. 4c, the NH$_3$ yield rate and FEs display a diminishing trend across the test potential range after the addition of TBA, particularly at lower potentials. The NH$_3$ yield rate and FEs were decreased from 2507.3 to 100.6 µg h^{-1} cm^{-2} and 94 to 17% at −0.05 V *vs.* RHE, respectively.

Notably, the NH$_3$ yield rate and FE of A-Ag@Ni/Ni(OH)$_2$ NWs decay are accompanied by the increase of NO$_2^-$ yield rate and FE (Fig. 4d), further proof that the introduction of TBA does not affect Ag NWs catalyzed conversion of NO$_3^-$ to NO$_2^-$. These comparisons clearly highlight the correlation between the kinetics of NO$_3$RR and the atomic H$_{ads}$, especially the conversion of NO$_2^-$ to NH$_3$.

3.5. Research on the reduction pathway of NO$_3$RR on the A-Ag@Ni/Ni(OH)$_2$ NWs

To elucidate the reduction pathway of NO$_3$RR on the A-Ag@Ni/Ni(OH)$_2$ NWs, in-situ Fourier-transform infrared (FTIR) measurements were conducted to monitor intermediates adsorbed on the electrode
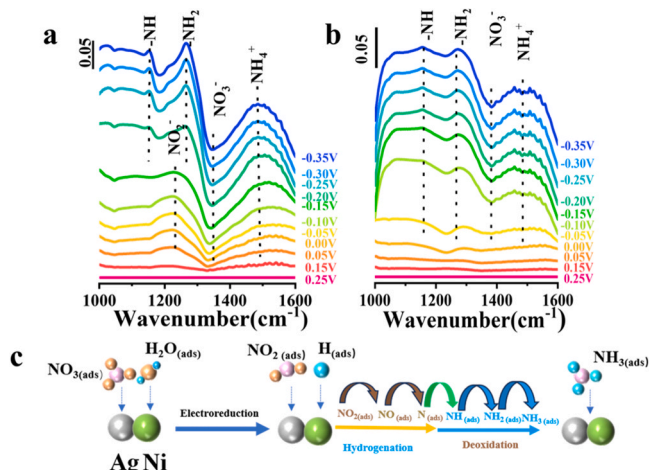

Fig. 5. Electrochemical in situ FTIR spectra of (a) A-Ag@Ni/Ni(OH)$_2$ NWs, and (b) Ag@Ni/Ni(OH)$_2$ NWs at different potentials in 1 M KOH and 0.1 M NO$_3^-$ solutions. (c) Schematic illustration of the proposed NO$_3$RR mechanism on A-Ag@Ni/Ni(OH)$_2$ NWs.
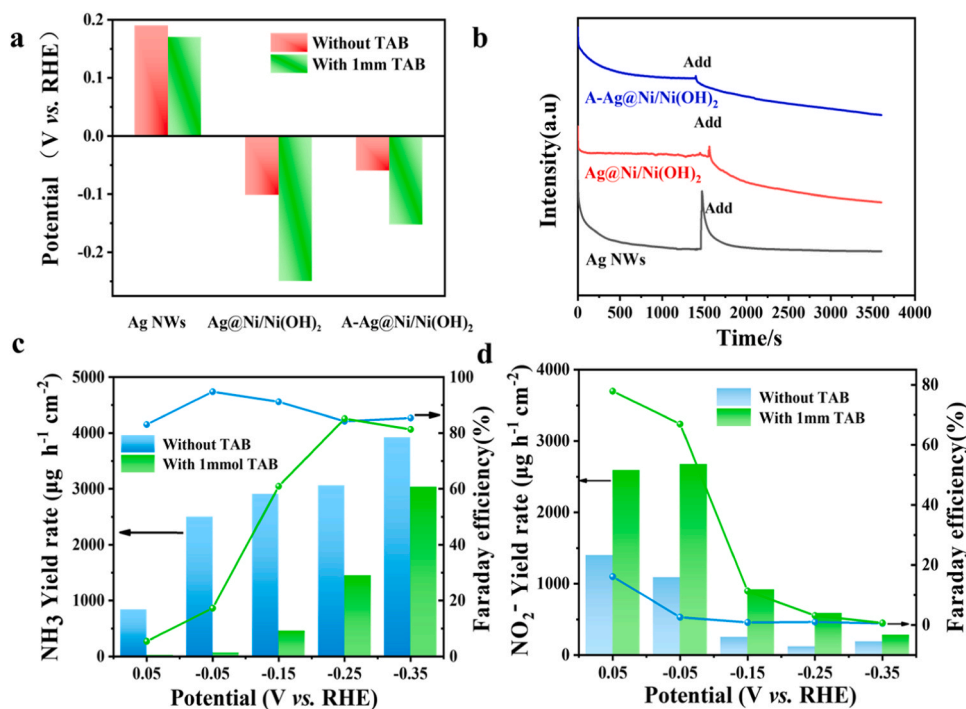

Fig. 4. (a) The LSV-derived potentials at a current density of −10 mA cm^{-2} and (b) *i-t* curves for NO$_3^-$ reduction without and with TBA on Ag NWs, Ag@Ni/Ni(OH)$_2$ NWs, A-Ag@Ni/Ni(OH)$_2$ NWs catalysts. (c) The NH$_3$ yields and FEs and (d) The NO$_2^-$ yields and FEs of Ag NWs, and A-Ag@Ni/Ni(OH)$_2$ NWs without and with TBA.

surface. Fig. 5a depicts a negative band at 1370 cm^{-1}, signifying the consumption of NO_3^-, observed at 0.05 V *vs.* RHE[78,81]. Concurrently, an escalating band at 1235 cm^{-1} is evident, correlating with the formation of NO_2^-[19,81]. Along with the appearance of NO_2^- peaks, three fragile bands at 1150, 1280, and 1452 cm^{-1} related to the NH, NH_2, and NH_4^+ formation were also observed [66,78,82]. Interestingly, the bands associated with the formation of NO_2^-, NH, NH_2, and NH_4^+ are observed at the same applied potential. The findings indicate that upon the formation of intermediate NO_2^-, a rapid kinetic process ensues, leading to NO_2^- conversion into the ultimate product NH_3 through the intermediates NH and NH_2. As the potential shifts negatively, the bands associated with NO_3^- consumption and the generation of $NH/NH_2/NH_4^+$ progressively intensify. Conversely, the band associated with NO_2^- production diminishes gradually and becomes barely discernible at −0.1 V *vs.* RHE. These observations indicate that at more negative potentials, the kinetics of NO_2^- conversion to NH_3 are further augmented, thereby impeding the accumulation of nitrite on the catalyst surface.

The FT-IR spectra collected on Ag@Ni/Ni(OH)$_2$ NWs were very similar to those of the A-Ag@Ni/Ni(OH)$_2$ NWs catalysts (Fig. 5b). Namely, the NO_3^- consumption and $NH/NH_2/NH_3$ generation take place concurrently. Differing from A-Ag@Ni/Ni(OH)$_2$ NWs catalysts, almost no band associated with NO_2^- has been detected. There are two primary reasons why NO_2^- cannot be detected on the surface of the Ag@Ni/Ni(OH)$_2$ NWs catalyst. Firstly, the Ag sites in the core are shielded by the outer shell Ni/Ni(OH)$_2$, resulting in low catalytic activity for converting NO_3^- to NO_2^- and thus a low concentration of NO_2^- on the catalyst surface. Secondly, the outer shell Ni/Ni(OH)$_2$ exhibits excellent electrocatalytic water splitting to produce H_{ads}. The generated H_{ads} then efficiently reduce NO_2^- to NH_3 through the H-assisted reduction pathway, resulting in a brief retention of NO_2^- on the electrode surface. Therefore, NO_2^- was not detected in the in situ infrared measurement. In addition, it is worth note that the formation of NH, NH_2, and NH_3 on Ag@Ni/Ni(OH)$_2$ NWs at −0.05 V was 100 mV more negative than that obtained on A-Ag@Ni/Ni(OH)$_2$ NWs. Moreover, the band at 1382 cm^{-1} correlated with NO_3^- consumption consistently exhibits fragility across the test potential range, indicating that the performance of NO$_3$RR catalyzed by Ag@Ni/Ni(OH)$_2$ NWs is constrained by the conversion of NO_3^- to NO_2^-. Despite the efficient generation of H_{ads} by the surface of Ag@Ni/Ni(OH)$_2$ NWs, which promotes the conversion of NO_2^- into NH_3. However, the Ag active sites are shielded by the Ni/Ni(OH)$_2$ phase, resulting in a scarcity of active sites for the adsorption of NO_3^- and converting it into NO_2^-, consequently diminishing the overall reaction rate of NO$_3$RR. Combining the reaction intermediate monitored by in-situ FTIR and the synergy between the Ag and Ni phases, the NO$_3$RR reaction pathways on A-Ag@Ni/Ni(OH)$_2$ NWs are summarized in Fig. 5c. Firstly, NO_3^- anions are adsorbed on the Ag sites to form $NO_3^-{}_{ads}$. The Ag serves as an active phase for catalyzing the conversion of $NO_3^-{}_{ads}$ to $NO_2^-{}_{ads}$. Meanwhile, the adsorbed H_2O molecules on Ni/Ni(OH)$_2$ sites are reduced to form active H_{ads}. Subsequently, the H_{ads} reduce $NO_2^-{}_{ads}$ to NH_3 step by step via a series of intermediates such as NH_{ads} and $NH_2{}_{ads}$.

3.6. Theoretical calculation investigation

Density-Functional Theory (DFT) calculations were performed to shed light on the synergistic effect between the Ag phase and the Ni/Ni(OH)$_2$ phase, further validating the advantage of the atomic H-mediated pathway responsible for the effective NO$_3$RR on A-Ag@Ni/Ni(OH)$_2$ NWs. Herein, the most stable and readily exposed Ag(111) surface is chosen as the structural model of silver phase, while the sampled Ni/Ni(OH)$_2$ interface features Ni anchored on the Ni(OH)$_2$ with defect sites by Ni–O bonds (Figure S26), as previously reported [83]. Both phases undertaking the evolutions of NO$_3$RR and H_2O splitting, respectively, have been comparatively investigated through the Gibbs free energy prifiles to establish the preferential reaction. Given that NO$_3$RR and H_2O splitting are competing reactions on the catalyst surface, which are unlikely

to occur simultaneously, once NO$_3$RR predominates, the process of H_2O splitting to produce H_{ads} will be inhibited, plaguing the H-assisted pathway of NO$_3$RR. Therefore, the electron reduction pathway (denoted as NO$_3$RR-1: $NO_3^- \rightarrow *NO_3^- \rightarrow *NO_2^- \rightarrow *NO \rightarrow *NOH \rightarrow *NHOH \rightarrow *NH_2OH \rightarrow *NH_2 \rightarrow *NH_3 \rightarrow NH_{3(g)}$) [12,82,84] is exclusively evaluated when analyzing the competition between NO$_3$RR and H_2O splitting on Ag and Ni phase, respectively.

Fig. 6a depicts the optimized structures of the intermediates and their relative Gibbs free energies along the NO$_3$RR-1 pathways on the Ag (111) surface, where the corresponding chemical equations are presented in Tables S2. In terms of thermodynamics, the sequencial reactions of $NO_3^- \rightarrow *NO_3^- \rightarrow *NO_2^-$ on Ag(111) proceed smoothly at 0 V *vs.* RHE, whereas the following $*NO_2^- \rightarrow *NO$ is significantly endothermic by 0.931 eV, which indicates that this transformation is restricted on the Ag(111) surface, resulting in the buildup of NO_2^- in the electrolyte. Such an observation further elucidates why Ag NWs promote the production of NO_2^- at low potentials. Subsequent conversion from *NO to *NOH gets even more endothermic by 1.08 eV, representing the rate-determining step (RDS), comparing to the slightly less endothermic step of *NOH → *NHOH by 0.713 eV. External potential is applied to neutralize the unfavored activation energy in the RDS, which is found to decrease as more negative potentials are applied, and eventually reaches a favorable range for NH_3 generation until the applied potential is −0.3 V *vs.* RHE, aligning with the experimental results. Specifically, Ag NWs demonstrate satisfactory performance in catalyzing NH_3 production at < −0.3 V *vs.* RHE. Comparatively, the ΔG diagram of H_2O splitting on the Ag(111) surface reveals a much higher barrier of 2 eV for H_2O splitting (Fig. 6b) to produce H_{ads}, indicating that NO$_3$RR primarily takes place on the Ag(111) surface, while the competing H_2O splitting is suppressed. Moreover, although *NO$_3$ can readily form on Ni/Ni(OH)$_2$ and be converted to *NO smoothly, further hydrogenation entails successively endothermic steps of *NO → *NOH → *NHOH by up to 2.05 eV (Fig. 6c), in sharp comparison to that of the H_2O splitting by as low as 0.98 eV (Fig. 6d), where Ni/Ni(OH)$_2$ preferably catalyzes the H_2O splitting reaction.

These results conclusively demonstrate that the primary function of the Ag-based phase in the A-Ag@Ni/Ni(OH)$_2$ NWs catalyst is to adsorb NO_3^- and promote its conversion into NH_3, whereas Ni/Ni(OH)$_2$ primarily handles the water splitting to generate H_{ads}. Facilitate by the enriched H_{ads} on the catalyst surface provided by Ni/Ni(OH)$_2$, the NO$_3$RR on the Ag (111) can undergo the H_{ads}-mediated pathways (denoted as NO$_3$RR-2: $NO_3^- \rightarrow *NO_3^- \rightarrow *NO_2^- \rightarrow *NO \rightarrow *N \rightarrow *NH \rightarrow *NH_2 \rightarrow *NH_3 \rightarrow NH_{3(g)}$) [20,25], where each step on Ag(111) turns out to be exothermic in the Gibbs free energy profile even at 0 V *vs.* RHE (Fig. 6e), demonstrating that NO$_3$RR-2 is thermodynamically more favorable than NO$_3$RR-1 when there is a sufficient amount of H_{ads} on the catalyst surface. Benifited from the synergistic effect by the introduction of Ni phase in providing H_{ads}, these calculations further substantiate that the Ag-based catalyst can achieve efficient conversion of NO_3^- to NH_3 through the H_{ads}-mediated pathway, rather than the electron reduction, which corroborates with the experimental rationality of the Ag-Ni interplay in effectively promoting NO$_3$RR.

4. Conclusion

In conclusion, the A-Ag@Ni/Ni(OH)$_2$ NWs with atomic-level Ag/Ni interfaces were successfully designed and synthesized. The synergy between Ag and Ni phases can reduce the high energy barrier of the NO_2^--to-NH_3 conversion steps on the Ag phase and the initial NO_3^- adsorption step on the Ni phase. Specially, Ag sites could afford active centers for the adsorption of NO_3^- and convert it to NO_2^-. Furthermore, Ni/Ni(OH)$_2$ sites as vibrant centers for accumulating atomic H_{ads}, facilitating the rapid conversion of NO_2^- to NH_3 via the H_{ads}-mediated pathway. DFT calculations further substantiate that the H_{ads}-mediated pathway is thermodynamically more favorable than the electron reduction pathway. The preferred H_{ads}-mediated pathway is revealed to benefit
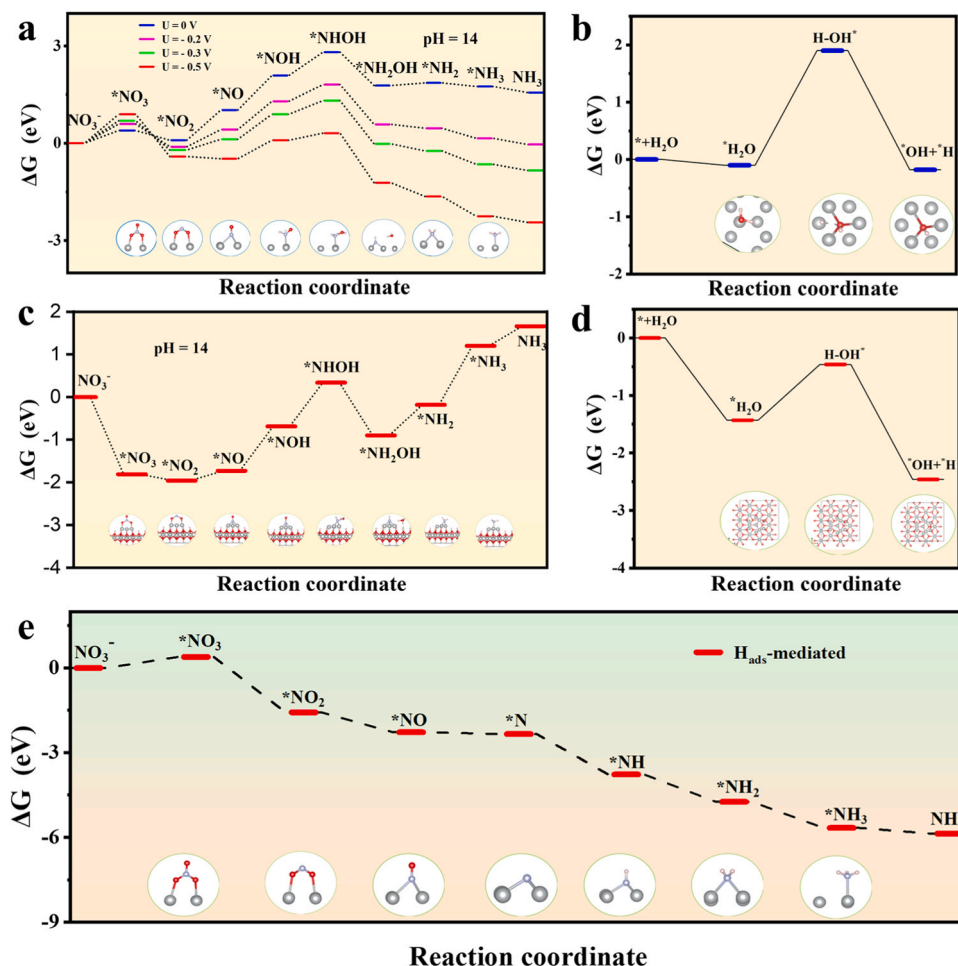
Fig. 6. Calculated Gibbs free energy diagrams of the NO$_3$RR and H$_2$O splitting pathways. The electron reduction pathways of NO$_3$RR on (a) the Ag(111) at different potentials and on (c) the Ni/Ni(OH)$_2$, the H$_2$O splitting pathways on (b) the Ag(111) and (d) the Ni/Ni(OH)$_2$, and (e) the H$_{ads}$-mediated pathway of NO$_3$RR on the Ag (111) at 0 V *vs.* RHE.

the generation of NH$_3$ and is an energy-efficient process, endowing the A-Ag@Ni/Ni(OH)$_2$ NWs with outstanding electrocatalytic activity and selectivity for the NO$_3^-$-to-NH$_3$ transformation at low potential. The NH$_3$ yield, FE, and NH$_3$ selectivity reach 2507.3 μg h^{-1} cm^{-2}, 92.3%, and 95.14% in 1 M KOH + 0.1 M KNO$_3$ solution at —0.05 V *vs.* RHE. The study may pave the way for a new approach in the rational design of electrocatalysts with desired functionalities for NO$_3$RR through the H$_{ads}$-mediated pathway.

Supporting information

Supporting Information is available from in the online version.

CRediT authorship contribution statement

Zhi Yang: Writing – review & editing. **Yingyang Jiang:** Conceptualization. **Jia Guan:** Software. **Yongjie Ge:** Writing – review & editing, Writing – original draft, Methodology, Investigation. **Hao Tang:** Software. **Jinjie Qian:** Formal analysis. **Xuemei Zhou:** Formal analysis. **Ling Ye:** Conceptualization. **Peng Xu:** Conceptualization. **Shilu Wu:** Data curation. **Longlong Huang:** Formal analysis. **Huagui Nie:** Writing – review & editing. **Deqing Kong:** Software.

Declaration of Competing Interest

The authors declare no conflict of interest.

Declaration of Competing Interest

The authors declare that they have no known competing financial interests or personal relationships that could have appeared to influence the work reported in this paper.

Data Availability

Data will be made available on request.

Appendix A. Supporting information

Supplementary data associated with this article can be found in the online version at doi:10.1016/j.apcatb.2024.124224.

References

[1] S. Sarkar, A. Adalder, S. Paul, S. Kapse, R. Thapa, U.K. Ghorai, Iron phthalocyanine hollow architecture enabled ammonia production via nitrate reduction to achieve

100% faradaic efficiency, Appl. Catal. B Environ. 343 (2024) 123580, https://doi.org/10.1016/j.apcatb.2023.123580.

[2] R.F. Service, Science, Liq. Sunshine 361 (2018) 120–123, https://doi.org/10.1126/science.361.6398.120.

[3] O. Elishav, B.M. Lis, E.M. Miller, D.J. Arent, A. Valera-Medina, A.G. Dana, G. E. Shter, G.S. Grader, Progress and prospective of nitrogen-based alternative fuels, Chem. Rev. 120 (2020) 5352–5436, https://doi.org/10.1021/acs.chemrev.9b00538.

[4] J. Li, G. Zhan, J. Yang, F. Quan, C. Mao, Y. Liu, Efficient ammonia electrosynthesis from nitrate on strained ruthenium nanoclusters, J. Am. Chem. Soc. 142 (15) (2020) 7036–7046, https://doi.org/10.1021/jacs.0c00418.

[5] N.C. Kani, N.H.L. Nguyen, K. Markel, R.R. Bhawnani, B. Shindel, K. Sharma, S. Kim, V.P. Dravid, V. Berry, Gauthier, Electrochemical reduction of nitrates on CoO nanoclusters-functionalized graphene with highest mass activity and nearly 100% selectivity to ammonia, Adv. Energy Mater. 13 (2023) 2204236, https://doi.org/10.1002/aenm.202204236.

[6] B.H.R. Suryanto, H.-L. Du, D. Wang, J. Chen, A.N. Simonov, D.R. MacFarlane, Challenges and prospects in the catalysis of electroreduction of nitrogen to ammonia, Nat. Catal. 2 (2019) 290–296, https://doi.org/10.1038/s41929-019-0252-4.

[7] G.-F. Chen, Y. Yuan, H. Jiang, S.-Y. Ren, L.-X. Ding, L. Ma, T. Wu, J. Lu, H. Wang, Electrochemical reduction of nitrate to ammonia via direct eight-electron transfer using a copper-molecular solid catalyst, Nat. Energy 5 (2020) 605–613, https://doi.org/10.1038/s41560-020-0654-1.

[8] J. Li, G. Zhan, J. Yang, F. Quan, C. Mao, Y. Liu, B. Wang, F. Lei, L. Li, A.W.M. Chan, L. Xu, Y. Shi, Y. Du, W. Hao, P.K. Wong, J. Wang, S.-X. Dou, L. Zhang, J.C. Yu, Efficient ammonia electrosynthesis from nitrate on strained ruthenium nanoclusters, J. Am. Chem. Soc. 142 (2020) 7036–7046, https://doi.org/10.1021/jacs.0c00418.

[9] W. Kang, L. Yan, J. Tang, S. Wu, H. Yu, Z. Li, Electrochemical activation of graphite electrode for nitrate reduction: Energetic performance and application potential, Appl. Catal. B Environ. 329 (2023) 122553, https://doi.org/10.1016/j.apcatb.2023.122553.

[10] A.C.A.D. Vooys, R.A.V. Santen, J.A.R.V. Veen, Electrocatalytic reduction of NO_3^- on palladium/copper electrodes, J. Mol. Catal. A-Chem. 154 (2000) 203–215, https://doi.org/10.1016/s1381-1169(99)00375-1.

[11] J. Zhou, F. Pan, Q. Yao, Y. Zhu, H. Ma, J. Niu, J. Xie, Achieving efficient and stable electrochemical nitrate removal by in-situ reconstruction of Cu_2O/Cu electroactive nanocatalysts on Cu foam, Appl. Catal. B Environ. 317 (2022) 121811, https://doi.org/10.1016/j.apcatb.2022.121811.

[12] T. Hu, C. Wang, M. Wang, C.M. Li, C. Guo, Theoretical insights into superior nitrate reduction to ammonia performance of copper catalysts, ACS Catal. 11 (2021) 14417–14427, https://doi.org/10.1021/acscatal.1c03666.

[13] T. Feng, J. Wang, Y. Wang, C. Yu, X. Zhou, B. Xu, K. Laszlo, F. Li, W. Zhang, Selective electrocatalytic reduction of nitrate to dinitrogen by Cu_2O nanowires with mixed oxidation-state, Chem. Eng. J. 433 (2022) 133495, https://doi.org/10.1016/j.cej.2021.133495.

[14] J. Cai, Y. Wei, A. Cao, J. Huang, Z. Jiang, S. Lu, S.-Q. Zang, Electrocatalytic nitrate-to-ammonia conversion with ~100% faradaic efficiency via single-atom alloying, Appl. Catal. B Environ. 316 (2022) 121683, https://doi.org/10.1016/j.apcatb.2022.121683.

[15] I. Katsounaros, G. Kyriacou, Influence of nitrate concentration on its electrochemical reduction on tin cathode: Identification of reaction intermediates, Electrochim. Acta 53 (2008) 5477–5484, https://doi.org/10.1016/j.electacta.2008.03.018.

[16] F.T. Bonner, M.N. Hughes, The aqueous solution chemistry of nitrogen in low positive oxidation states, J. Chemin.-. 7 (1989) 215–234, https://doi.org/10.1002/chin.198906328.

[17] J.F.E. Gootzen, P.G.J.M. Peeters, J.M.B. Dukers, L. Lefferts, W. Visscher, J.A.R. V. Veen, ChemInform Abstract: The electrocatalytic reduction of NO_3^- on Pt, Pd and Pt + Pd electrodes activated with Ge, J. Chemin.-. 434 (1998) 171–183, https://doi.org/10.1002/chin.199809008.

[18] J.-X. Liu, D. Richards, N. Singh, B.R. Goldsmith, Activity and selectivity trends in electrocatalytic nitrate reduction on transition metals, ACS Catal. 9 (2019) 7052–7064, https://doi.org/10.1021/acscatal.9b02179.

[19] Y. Wang, C. Wang, M. Li, Y. Yu, B. Zhang, Nitrate electroreduction: mechanism insight, in situ characterization, performance evaluation, and challenges, Chem. Soc. Rev. 50 (2021) 6720–6733, https://doi.org/10.1039/d1cs00116g.

[20] D. Xu, Y. Li, L. Yin, Y. Ji, J. Niu, Y. Yu, Electrochemical removal of nitrate in industrial wastewater, Front. Environ. Sci. Eng. 12 (2018) 1–14, https://doi.org/10.1007/s11783-018-1033-z.

[21] J. Gao, B. Jiang, C. Ni, Y. Qi, X. Bi, Enhanced reduction of nitrate by noble metal-free electrocatalysis on P doped three-dimensional Co_3O_4 cathode: Mechanism exploration from both experimental and DFT studies, Chem. Eng. J. 382 (2019) 123034, https://doi.org/10.1016/j.cej.2019.123034.

[22] J. Martinez, A. Ortiz, I. Ortiz, State-of-the-art and perspectives of the catalytic and electrocatalytic reduction of aqueous nitrates, Appl. Catal. B Environ. 207 (2017) 42–59, https://doi.org/10.1016/j.apcatb.2017.02.016.

[23] J. Zhou, M. Wen, R. Huang, Q. Wu, Y. Luo, Y. Tian, G. Wei, Y. Fu, Regulating active hydrogen adsorbed on grain boundary defects of nano-nickel for boosting ammonia electrosynthesis from nitrate, Energ. Environ. Sci. 16 (2023) 2611–2620, https://doi.org/10.1039/d2ee04095f.

[24] W. Fu, X. Du, P. Su, Q. Zhang, M. Zhou, Synergistic effect of Co(III) and Co(II) in a 3D structured Co_3O_4/Carbon felt electrode for enhanced electrochemical nitrate reduction reaction, ACS Appl. Mater. Inter. 13 (2021) 28348–28358, https://doi.org/10.1021/acsami.1c07063.

[25] W. Zheng, L. Zhu, Z. Yan, Z. Lin, Z. Lei, Y. Zhang, H. Xu, Z. Dang, C. Wei, C. Feng, Self-activated ni cathode for electrocatalytic nitrate reduction to ammonia: from fundamentals to scale-up for treatment of industrial wastewater, Environ. Sci. Technol. 55 (2021) 13231–13243, https://doi.org/10.1021/acs.est.1c02278.

[26] H. Liu, J. Park, Y. Chen, Y. Qiu, Y. Cheng, K. Srivastava, S. Gu, B.H. Shanks, L. T. Roling, W. Li, Electrocatalytic nitrate reduction on oxide-derived silver with tunable selectivity to nitrite and ammonia, ACS Catal. 11 (2021) 8431–8442, https://doi.org/10.1021/acscatal.1c01525.

[27] Y. Wang, A. Xu, Z. Wang, L. Huang, J. Li, F. Li, J. Wicks, M. Luo, D.-H. Nam, C.-S. Tan, Y. Ding, J. Wu, Y. Lum, D. Cao-Thang, D. Sinton, G. Zheng, E.H. Sargent, Enhanced nitrate-to-ammonia activity on copper-nickel alloys via tuning of intermediate adsorption, J. Am. Chem. Soc. 142 (2020) 5702–5708, https://doi.org/10.1021/jacs.9b13347.

[28] Y. Xu, K. Ren, T. Ren, M. Wang, S. Yu, Z. Wang, X. Li, L. Wang, H. Wang, Phosphorus-triggered modification of the electronic structure and surface properties of Pd_4S nanowires for robust hydrogen evolution electrocatalysis, J. Mater. Chem. A. 8 (2020) 19873–19878, https://doi.org/10.1039/D0TA07403A.

[29] Y. Deng, S. Yin, Y. Liu, Y. Lu, X. Cao, L. Wang, H. Wang, Y. Zhao, H. Gu, Mesoporous AgPdPt nanotubes as electrocatalysts for the oxygen reduction reaction, ACS Appl. Nano Mater. 2 (2019) 1876, https://doi.org/10.1021/acsanm.8b02206.

[30] A. Yu, C. Lee, N.-S. Lee, M.H. Kim, Y. Lee, Highly efficient silver-cobalt composite nanotube electrocatalysts for favorable oxygen reduction reaction, ACS Appl. Mater. Inter. 8 (2016) 32833–32841, https://doi.org/10.1021/acsami.6b11073.

[31] W. Zhong, W. Li, C. Yang, J. Wu, R. Zhao, M. Idrees, H. Xiang, Q. Zhang, X. Li, Interfacial electron rearrangement: Ni activated $Ni(OH)_2$ for efficient hydrogen evolution, J. Energy Chem. 61 (2021) 236–242, https://doi.org/10.1016/j.jechem.2021.02.013.

[32] Y. Tang, L. Dong, H.B. Wu, X.-Y. Yu, Tungstate-modulated $Ni/Ni(OH)_2$ interface for efficient hydrogen evolution reaction in neutral media, J. Mater. Chem. A. 9 (2021) 1456–1462, https://doi.org/10.1039/d0ta09749g.

[33] K.E. Korte, S.E. Skrabalak, Y. Xia, Rapid synthesis of silver nanowires through a CuCl- or $CuCl_2$-mediated polyol process, J. Mater. Chem. 18 (2008) 437–441, https://doi.org/10.1039/b714072j.

[34] W.M. Schuette, W.E. Buhro, Silver chloride as a heterogeneous nucleant for the growth of silver nanowires, ACS Nano 7 (2013) 3844–3853, https://doi.org/10.1021/nn400414h.

[35] Y. Zhao, R. Shi, X. Bian, C. Zhou, Y. Zhao, S. Zhang, F. Wu, G.I.N. Waterhouse, L.-Z. Wu, C.-H. Tung, T. Zhang, Ammonia detection methods in photocatalytic and electrocatalytic experiments: how to improve the reliability of NH_3 production rates, Adv. Sci. 6 (2019) 1802109, https://doi.org/10.1002/advs.201802109.

[36] J. Wang, L. Yu, L. Hu, G. Chen, H. Xin, X. Feng, Ambient ammonia synthesis via palladium-catalyzed electrohydrogenation of dinitrogen at low overpotential, Nat. Commun. 9 (2018) 1795, https://doi.org/10.1038/s41467-018-04213-9.

[37] J.-Y. Fang, Q.-Z. Zheng, Y.-Y. Lou, K.-M. Zhao, S.-N. Hu, G. Li, O. Akdim, X.-Y. Huang, S.-G. Sun, Ampere-level current density ammonia electrochemical synthesis using CuCo nanosheets simulating nitrite reductase bifunctional nature, Nat. Commun. 13 (2022) 7899, https://doi.org/10.1038/s41467-022-35533-6.

[38] L. Sun, B. Liu, Mesoporous PdN alloy nanocubes for efficient electrochemical nitrate reduction to ammonia, Adv. Mater. 35 (2023) 2207305, https://doi.org/10.1002/adma.202207305.

[39] J. Huang, J. Sheng, R.D. Ross, J. Han, X. Wang, B. Song, S. Jin, Modifying redox properties and local bonding of Co_3O_4 by CeO_2 enhances oxygen evolution catalysis in acid, Nat. Commun. 12 (2021) 3036, https://doi.org/10.1038/s41467-021-23390-8.

[40] G. Kresse, J. Furthmüller, Efficient iterative schemes for ab initio total-energy calculations using a plane-wave basis set, Phys. Rev. B. 54 (1996) 11169, https://doi.org/10.1103/PhysRevB.54.11169.

[41] G. Kresse, J. Furthmüller, Efficiency of ab-initio total energy calculations for metals and semiconductors using a plane-wave basis set, Comp. Mater. Sci. 6 (1996) 15–50, https://https://doi.org/10.1016/0927-0256(96)00008-0.

[42] G. Kresse, D. Joubert, From ultrasoft pseudopotentials to the projector augmented-wave method, Phys. Rev. B. 59 (1999) 1758, https://doi.org/10.1103/PhysRevB.59.1758.

[43] P.E. Blöchl, Projector augmented-wave method, Phys. Rev. B. 50 (1994) 17953, https://doi.org/10.1103/PhysRevB.50.17953.

[44] J.P. Perdew, K. Burke, M. Ernzerhof, Generalized gradient approximation made simple, Phys. Rev. Lett. 77 (1996) 3865, https://doi.org/10.1103/PhysRevLett.77.3865.

[45] H.A. Atwater, B.M. Kayes, N.S. Lewis, Structures of ordered arrays of semiconductors. U.S. Patent Application No. 12/176,057.

[46] Y. Ren, F. Tian, L. Jin, Y. Wang, J. Yang, S. You, Y. Liu, Fluidic MXene electrode functionalized with iron single atoms for selective electrocatalytic nitrate transformation to ammonia, Rev. Environ. Sci. Bio 57 (2023) 10458–10466, https://doi.org/10.1021/acs.est.3c02520.

[47] P.W. Atkins, Physical Chemistry, 485, Oxford University Press, Oxford, U.K., 1998, pp. 925–927, 942.

[48] P.J. Linstrom, W.G. Mallard, The NIST Chemistry WebBook: A chemical data resource on the internet, J. Chem. Eng. Data 46 (2001) 1059–1063, https://doi.org/10.1021/je000236i.

[49] Á. Valdés, Z.-W. Qu, G.-J. Kroes, J. Rossmeisl, J.K. Nørskov, Oxidation and photo-oxidation of water on TiO_2 surface, J. Phys. Chem. C. 112 (2008) 9872–9879, https://doi.org/10.1021/jp711929d.

[50] J. Dean, J. A, Lange's Handbook of Chemistry (16th Edition), McGraw-Hill, New York, 1999.

[51] J.K. Nørskov, J. Rossmeisl, A. Logadottir, L. Lindqvist, J.R. Kitchin, T. Bligaard, H. Jonsson, Origin of the overpotential for oxygen reduction at a fuel-cell cathode, J. Phys. Chem. B 108 (2004) 17886–17892, https://doi.org/10.1021/jp047349j.

[52] R. Rajendiran, P.K. Seelam, A. Patchaiyappan, P. Balla, H. Shankar, B. Ravi, V. Perupogu, U. Lassi, Morphologically tailored facet dependent silver nanoparticles supported α-Al$_2$O$_3$ catalysts for chemoselective reduction of aromatic nitro compounds, Chem. Eng. J. 451 (2023) 138507, https://doi.org/10.1016/j.cej.2022.138507.

[53] S. Lu, B. Zhao, M. Chen, L. Wang, X.-Z. Fu, J.-L. Luo, Electrodeposited porous spherical Ni(OH)$_2$@Ni on carbon paper for high-efficiency hydrogen evolution, J. Hydrog. Energy 46 (2021) 1540–1547, https://doi.org/10.1016/j.ijhydene.2020.10.126.

[54] B. Lin, Z. Bao, A. Wang, Y. Ding, W. Zhan, L. Wang, Y. Guo, Q. Dai, Y. Guo, F. Gao, An efficient Co-Ni hydrous oxide catalyst for elimination of NO pollutant in semi-enclosed spaces at ambient temperature, Appl. Catal. B Environ. 337 (2023), https://doi.org/10.1016/j.apcatb.2023.122984.

[55] A.I. Yanson, P. Rodriguez, N. Garcia-Araez, R.V. Mom, F.D. Tichelaar, M.T. Koper, Cathodic corrosion: a quick, clean, and versatile method for the synthesis of metallic nanoparticles, Angew. Chem. Int. Ed. 50 (2011) 6346, https://doi.org/10.1002/anie.201100471.

[56] A. Yanson, Y.I. Yanson, Cathodic corrosion. II. Properties of nanoparticles synthesized by cathodic corrosion, Low. Temp. Phys. 39 (2013) 312–317, https://doi.org/10.1063/1.4795197.

[57] P. Rodriguez, F.D. Tichelaar, M.T. Koper, A.I. Yanson, Cathodic corrosion as a facile and effective method to prepare clean metal alloy nanoparticles, J. Am. Chem. Soc. 133 (2011) 17626–17629, https://doi.org/10.1021/ja208264e.

[58] E. Bennett, J. Monzo, J. Humphrey, D. Plana, M. Walker, C. McConville, D. Fermin, A. Yanson, P. Rodriguez, A synthetic route for the effective preparation of metal alloy nanoparticles and their use as active electrocatalysts, ACS Catal. 6 (2016) 1533–1539, https://doi.org/10.1021/acscatal.5b02598.

[59] J. Yu, J. Xiong, B. Cheng, S. Liu, Fabrication and characterization of Ag–TiO$_2$ multiphase nanocomposite thin films with enhanced photocatalytic activity, Appl. Catal. B Environ. 60 (2005) 211–221, https://doi.org/10.1016/j.apcatb.2005.03.009.

[60] E. Murphy, Y. Liu, I. Matanovic, M. Ruescher, Y. Huang, A. Ly, S. Guo, W. Zang, X. Yan, A. Martini, J. Timoshenko, B.R. Cuenya, I.V. Zenyuk, X. Pan, E.D. Spoerke, P. Atanassov, Elucidating electrochemical nitrate and nitrite reduction over atomically-dispersed transition metal sites, Nat. Commun. 14 (2023) 4554, https://doi.org/10.1038/s41467-023-40174-4.

[61] C. Choi, J. Cai, C. Lee, H.M. Lee, M. Xu, Y. Huang, Intimate atomic Cu-Ag interfaces for high CO$_2$RR selectivity towards CH$_4$ at low over potential, Nano Res. 14 (2021) 3497–3501, https://doi.org/10.1007/s12274-021-3639-x.

[62] Y. Guo, R. Zhang, S. Zhang, Y. Zhao, Q. Yang, Z. Huang, B. Dong, C. Zhi, Pd doping-weakened intermediate adsorption to promote electrocatalytic nitrate reduction on TiO$_2$ nanoarrays for ammonia production and energy supply with zinc–nitrate batteries, Energ. Environ. Sci. 14 (2021) 3938–3944, https://doi.org/10.1039/d1ee00806d.

[63] F. Zhao, G. Hai, X. Li, Z. Jiang, H. Wang, Enhanced electrocatalytic nitrate reduction to ammonia on cobalt oxide nanosheets via multiscale defect modulation, Chem. Eng. J. 461 (2023) 141960, https://doi.org/10.1016/j.cej.2023.141960.

[64] H. Jiang, G.-F. Chen, O. Savateev, J. Xue, L.-X. Ding, Z. Liang, M. Antonietti, H. Wang, Enabled efficient ammonia synthesis and energy supply in a zinc-nitrate battery system by separating nitrate reduction process into two stages, Angew. Chem. Int. Ed. 62 (2023) e202218717, https://doi.org/10.1002/anie.202218717.

[65] H.-Y. Yang, K.-Y. He, X. Ai, X. Liu, Y. Yang, S.-B. Yin, P.-J. Jin, Y. Chen, Pyridine functionalized silver nanosheets for nitrate electroreduction, J. Mater. Chem. A. 11 (2023) 16068–16073, https://doi.org/10.1039/d3ta03467d.

[66] L. Huang, L. Cheng, T. Ma, J.-J. Zhang, H. Wu, J. Su, Y. Song, H. Zhu, Q. Liu, M. Zhu, Z. Zeng, Q. He, M.-K. Tse, D.-t Yang, B.I. Yakobson, B.Z. Tang, Y. Ren, R. Ye, Direct synthesis of ammonia from nitrate on amorphous graphene with near 100% efficiency, Adv. Mater. 35 (2023) 2211856. ⟨https://10.1002/adma.202211856⟩.

[67] W.J. Sun, H.Q. Ji, L.X. Li, H.Y. Zhang, Z.K. Wang, J.H. He, J.M. Lu, Built-in electric field triggered interfacial accumulation effect for efficient nitrate removal at ultra-low concentration and electroreduction to ammonia, Angew. Chem. Int. Ed. 60 (2021) 22933–22939, https://doi.org/10.1002/anie.202109785.

[68] W. Gao, K. Xie, J. Xie, X. Wang, H. Zhang, S. Chen, H. Wang, Z. Li, C. Li, Alloying of Cu with Ru enabling the relay catalysis for reduction of nitrate to ammonia, Adv. Mater. 35 (2023) 2202952, https://doi.org/10.1002/adma.202202952.

[69] Y. Huang, J. Long, Y. Wang, N. Meng, Y. Yu, S. Lu, J. Xiao, B. Zhang, Engineering nitrogen vacancy in polymeric carbon nitride for nitrate electroreduction to ammonia, ACS Appl. Mater. Inter. 13 (2021) 54967–54973, https://doi.org/10.1021/acsami.1c15206.

[70] R. Jia, Y. Wang, C. Wang, Y. Ling, Y. Yu, B. Zhang, Boosting selective nitrate electroreduction to ammonium by constructing oxygen vacancies in TiO$_2$, ACS Catal. 10 (2020) 3533–3540, https://doi.org/10.1021/acscatal.9b05260.

[71] T. Ren, K. Ren, M. Wang, M. Liu, Z. Wang, H. Wang, X. Li, L. Wang, Y. Xu, Concave-convex surface oxide layers over copper nanowires boost electrochemical nitrate-to-ammonia conversion, Chem. Eng. J. 426 (2021) 130759, https://doi.org/10.1016/j.cej.2021.130759.

[72] C. Wang, Z. Liu, T. Hu, J. Li, L. Dong, F. Du, C. Li, C. Guo, Metasequoia-like nanocrystal of iron-doped copper for efficient electrocatalytic nitrate reduction into ammonia in neutral media, Chemsuschem 14 (2021) 1825–1829, https://doi.org/10.1002/cssc.202100127.

[73] Y. Wang, W. Zhou, R. Jia, Y. Yu, B. Zhang, Unveiling the activity origin of a copper-based electrocatalyst for selective nitrate reduction to ammonia, Angew. Chem. Int. Ed. 59 (2020) 5350–5354, https://doi.org/10.1002/anie.201915992.

[74] W. Wen, P. Yan, W. Sun, Y. Zhou, X.Y. Yu, Metastable phase Cu with optimized local electronic state for efficient electrocatalytic production of ammonia from nitrate, Adv. Funct. Mater. 33 (2023) 2212236, https://doi.org/10.1002/adfm.202212236.

[75] Y. Xu, Y. Sheng, M. Wang, T. Ren, K. Shi, Z. Wang, X. Li, L. Wang, H. Wang, Interface coupling induced built-in electric fields boost electrochemical nitrate reduction to ammonia over CuO@MnO$_2$ core-shell hierarchical nanoarrays, J. Mater. Chem. A. 10 (2022) 16883–16890, https://doi.org/10.1039/d2ta02006h.

[76] H. Yin, Y. Peng, J. Li, Electrocatalytic reduction of nitrate to ammonia via a Au/Cu single atom alloy catalyst, Environ. Sci. Technol. 57 (2023) 3134–3144, https://doi.org/10.1021/acs.est.2c07968.

[77] G. Zhang, X. Li, K. Chen, Y. Guo, D. Ma, K. Chu, Tandem electrocatalytic nitrate reduction to ammonia on mbenes, Angew. Chem. Int. Ed. 62 (2023) e202300054, https://doi.org/10.1002/anie.202300054.

[78] G.E. Dima, A.C.A. De Vooys, M.T.M. Koper, Electrocatalytic reduction of nitrate at low concentration on coinage and transition-metal electrodes in acid solutions, J. Electroanal. Chem. 554 (2003) 15–23, https://doi.org/10.1016/s0022-0728(02)01443-2.

[79] W. He, J. Zhang, S. Dieckhoefer, S. Varhade, A.C. Brix, A. Lielpetere, S. Seisel, J.R.C. Junqueira, W. Schuhmann, Splicing the active phases of copper/cobalt-based catalysts achieves high-rate tandem electroreduction of nitrate to ammonia, Nat. Commun. 13 (2022) 1129, https://doi.org/10.1038/s41467-022-28728-4.

[80] G. Jiang, M. Lan, Z. Zhang, X. Lv, Z. Lou, X. Xu, F. Dong, S. Zhang, Identification of active hydrogen species on palladium nanoparticles for an enhanced electrocatalytic hydrodechlorination of 2, 4-dichlorophenol in water, Environ. Sci. Technol. 51 (2017) 7599–7605, https://doi.org/10.1021/acs.est.7b01128.

[81] E. Perez-Gallent, M.C. Figueiredo, I. Katsounaros, M.T.M. Koper, Electrocatalytic reduction of nitrate on copper single crystals in acidic and alkaline solutions, Electrochim. Acta 227 (2017) 77–84, https://doi.org/10.1016/j.electacta.2016.12.147.

[82] D. Hao, Z.-G. Chen, M. Figiela, I. Stepniak, W. Wei, B.-J. Ni, Emerging alternative for artificial ammonia synthesis through catalytic nitrate reduction, J. Mater. Sci. Technol. 77 (2021) 163–168, https://doi.org/10.1016/j.jmst.2020.10.056.

[83] W. Zhong, W. Li, C. Yang, J. Wu, R. Zhao, M. Idrees, H. Xiang, Q. Zhang, X. Li, Interfacial electron rearrangement: Ni activated Ni(OH)$_2$ for efficient hydrogen evolution, J. Energy Chem. 61 (2021) 236–242, https://doi.org/10.1016/j.jechem.2021.02.013.